ARTICLE

Martin Oheim · Walter Stühmer

Tracking chromaffin granules on their way through the actin cortex

Abstract Quantitative time-lapse evanescent-wave imaging of individual fluorescently labelled chromaffin granules was used for kinetic analysis of granule trafficking through a ~300-nm ($1/e^2$) optical section beneath the plasma membrane. The mean squared displacement (MSD) was used to estimate the three-dimensional diffusion coefficient ($D^{(3)}$). We calculated the granules' speed, frame-to-frame displacement and direction and their autocorrelation to identify different stages of approach to the membrane. $D^{(3)}$ was about 10,000 times lower than expected for free diffusion. Granules located ~60 nm beneath the plasma membrane moved on random tracks ($D^{(3)} \approx 10^{-10} \, \mathrm{cm^2 \, s^{-1}}$) with several reversals in direction before they approached their docking site at angles larger than 45°. Docking was observed as a loss of vesicle mobility by two orders of magnitude within <100 ms. For longer observation times the MSD saturated, as if the granules' movement was confined to a volume only slightly larger than the granule. Rarely, the local random motion was superimposed with a directed movement in a plane beneath the membrane. Stimulation of exocytosis selectively depleted the immobile, near-membrane granule population and caused a recruitment of distant granules to sites at the plasma membrane. Their absolute mobility levels were not significantly altered. Application of latrunculin or jasplakinolide to change F-actin polymerisation caused a change in $D^{(3)}$ of the mobile granule population as well as a reduction of the rate of release, suggesting that granule mobility is constrained by the filamentous actin meshwork and that stimulation-dependent changes in actin viscosity propel granules through the actin cortex.

Introduction

Cells release transmitters and hormones by exocytosis of vesicles or granules. For these organelles to be released, they must be delivered and tethered to the plasma membrane. Until recently, direct studies of the intracellular translocation, docking and maturation along the way towards exocytosis had not been posible (see, e.g., Burgoyne 1998; Burgoyne and Morgan 1998; Neher 1998). Indirect insight was gained from studying the depression of the secretory response in answer to repetitive or maintained stimulation (Betz 1970; Elmquist and Quastel 1965; Rosenmund and Stevens 1996; Stevens and Tsujimoto 1995). In simple kinetic models, vesicles are proposed to mature through a linear sequence of distinct states to acquire "fusion competence" (Heinemann et al. 1993). Different models have resulted in the definition of "pools" of granules in different degrees of "readiness" for release (Ämmälä et al. 1993; Bittner and Holz 1992b; Gillis and Chow 1997; Gillis and Misler 1993; Heinemann et al. 1993; Horrigan and Bookman 1994; Moser and Neher 1997; Oheim et al. 1999b; Smith et al. 1998).

Dissecting kinetic intermediates

While compartmental modelling provides a convenient way to explain dynamic changes in the rate of secretion (Neher 1998; Weis et al. 1999), the functional significance of "fusion competence", and what constitutes the different "reserve", "docked", "release-ready" and

M. Oheim[1] (✉) · W. Stühmer
Max-Planck Institute for Experimental Medicine,
Molecular Biology of Neuronal Signals,
Hermann Rein Strasse 3, 37075 Göttingen, Germany

Present address:
[1] Ecole Supérieure de Physique et Chimie Industrielles
de la Ville de Paris (ESPCI), Laboratoire de Neurophysiologie
et Nouvelles Microscopies, INSERM EPI 00-02,
10 Rue Vauquelin, 75005 Paris, France
e-mail: martin.oheim@espci.fr

"immediately releasable" granule and vesicle pools is less clear. The depression of the secretory response has been attributed to the depletion of a limited "pool" of release-ready vesicles located at or in the immediate vicinity of the plasma membrane (Almers 1990; Gillis and Chow 1997; Heinemann et al. 1993; Oheim et al. 1999b; Parsons et al. 1995a). Clostridial neurotoxins have served as molecular tools to dissect different stages of protein assembly (Bittner and Holz 1993; Glenn and Burgoyne 1996; Jahn and Niemann 1994; Penner et al. 1986; Xu et al. 1998), and have revealed important details on the "late" steps in secretion control. Temperature and intracellular components, e.g. ATP, change the speed of granule maturation (Bittner and Holz 1992a, 1992b; Jankowski et al. 1993; Lippincott-Schwartz et al. 1999; Parsons et al. 1995a, b), but their effects may be too unspecific to be used to study the transition from one particular state to another.

A role for the cytoskeleton?

Based on electron microscopical images (Aunis et al. 1979; Nakata and Hirokawa 1992; Plattner et al. 1997), a cortical-actin barrier has been proposed to regulate access to sites at the plasma membrane (Burgoyne and Cheek 1987; Cheek and Burgoyne 1986). Its reorganisation may involve changes in actin-filament cross-linking and interactions with the granule and the plasma membrane (reviewed by Fowler and Vale 1996) that directly regulate the size of the readily releasable pool (Vitale et al. 1995). As granules entangled in the actin cortex do not show up in standard assays for secretion, like capacitance measurements of the cell surface area, or the electrochemical detection of the released transmitter (Chow and von Rüden 1995; Gillis 1995), it is unclear whether cortical actin indeed acts as a physical barrier to prevent granule docking, or if its role is more a regulatory one, e.g. by transiently depolymerising during exocytosis (Burgoyne and Cheek 1987; Trifaró and Vitale 1993; Vitale et al. 1991).

Open questions

Despite considerable progress in the understanding of the cellular elements of secretion control (see, e.g., Neher 1998 for a recent review), the observation of constrained granule mobility (Oheim et al. 1999b; Steyer and Almers 1999; Steyer et al. 1997) has not yet resulted in a molecular model of why granule docking and fusion sites are so close together. Do granules diffuse through the cytoplasm and are captured near the release site, or does an active transport mechanism direct granules to these sites? Why are some sites at the membrane distinct from others (Oheim et al. 1999b; Schroeder et al. 1994), and how are granules targeted to them? It is unknown how long granules reside at the different pre-exocytotic stages, if only docked granules can acquire fusion

competence, and to which extent the "docking" reaction is reversible. Tracking of individual granules on their way through the actin cortex would be attractive to resolve some of these issues.

Evanescent wave fluorescence excitation

Direct observation of individual near-membrane chromaffin granules has become possible with the introduction of evanescent wave (EW) microscopy (see Axelrod et al. 1992; Oheim et al. 1999b for recent reviews) to studies of secretion (Johns et al. 1999; Lang et al. 1997; Oheim et al. 1998b, 1999b; Steyer et al. 1997) (Fig. 1). Dye-labelled granules show up as individual pinpoints (Fig. 1B) that can be tracked on a time-lapse image series (Oheim et al. 1999b; Steyer and Almers 1999). Whereas imaging with virtually no background, the use of wide-field detection, and the reduction of photodamage due to the confinement of excitation light constitute the foremost advantages for imaging individual granules, additional information about granule location is contained in the decay of the evanescent field intensity. With increasing separation distance from the reflecting interface the excitation intensity and hence the granule's fluorescence signal diminishes. The comparison of spot intensities at different times provides information about distances traversed by the granule in a direction normal to the interface (Oheim et al. 1999b; Steyer and Almers 1999; Steyer et al. 1997).

Calibrating evanescent wave excited fluorescence

The penetration depth – calculated from the knowledge of the excitation wavelength, incidence angle and estimates of the refractive indices at the interface – does not
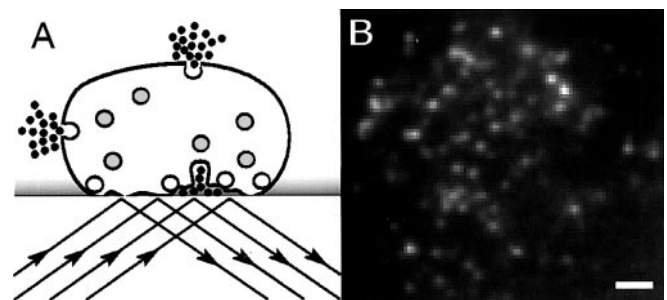

Fig. 1 A Principle of evanescent wave (EW) excitation. A light beam is directed on to a dielectric interface. Total internal reflection sets up a decaying near field that can be used to excite fluorescence, e.g., in dye-loaded chromaffin granules of cells grown on glass coverslips. Only granules close to the reflecting interface will fluoresce (*clear circles*), whereas those located deeper in the cell are not excited by the evanescent field (*grey circles*, drawing not to scale). **B** EW image at a calculated penetration depth of 120 nm. Individual vesicles appear as bright fluorescent spots in front of a dim background that is probably due to scattered excitation light and unspecific staining. The *scale bar* is 1 μm

suffice to unambiguously translate intensity changes into axial distance information. The distance estimate is entangled with the effects of photobleaching, changes in fluorophore concentration, and intensity changes resulting from the distance-dependent emission pattern of the fluorophore dipole close to the dielectric interface (Burghardt 1989; Burghardt and Thompson 1984; Carniglia et al. 1972; Drexhage 1970; Hellen and Axelrod 1987), as well as changes in the background fluorescence or the quantum yield of the dye. Single images can only provide measurements of one of these parameters if the others are assumed constant, or change slowly compared to the rate of image acquisition. Furthermore, scattering due to non-uniform cellular adhesion and intracellular dielectric boundaries causes a spread of the EW field. In the presence of dynamic changes in the cell's footprint topography it is difficult to distinguish changes in cell shape from local membrane dynamics. Finally, the opening of the fusion pore (Almers 1990) causes a modification of the local chemical environment owing to the collapse of the pH gradient between the acidic intravesicular compartment and the cell exterior.

Aims of the study

In this study, we present a simple way to directly view, at high temporal resolution, changes in granule position isolated from other parameters. We used EW microscopy to excite fluorescence in acridine orange-loaded large dense-core granules in live bovine adrenal chromaffin cells grown on BK-7 glass coverslips. Our goal was to optimise the optical sectioning, maximise the signal-background ratio and depth discrimination, and to minimise the effects of photo damage. Tracking relies on fitting two-dimensional (2-D) Gaussian distributions with the fluorescence distribution $F(x, y)$ of single spots in individual images. The resulting parameters (full-width-half-maximal diameter, and their peak and surrounding background intensities) are monitored over time. Comparing *relative* changes in fluorescence with respect to the *local* background intensity in the immediate proximity of a granule, our approach also allows the analysis of axial granule movement that otherwise cannot be distinguished from a cooperative movement of membrane patches. Lateral granule mobility is studied using single-particle algorithms based on the tracking of the "centre-of-mass" of fluorescence of the granule (Gosh and Webb 1994).

Using this improvement of EW imaging, we measured the frequency of fusion events at individual sites of release and the angle-of-approach to the membrane. We studied the velocity profile of granular mobility, as well as the dwell time in different pre-exocytic states. We distinguished different modes of mobility and compare these findings for unstimulated cells and after membrane depolarisations. To relate granule mobility to cell biological processes we tested the effect of chemical compounds interfering with actin polymerisation. We propose a model for granular motility in the immediate proximity of the membrane.

Materials and methods

Cell preparation and labelling of chromaffin granules

Bovine adrenal glands were obtained from a local slaughterhouse and immediately used for cell preparation. Cells were isolated as previously described (Oheim et al. 1998b) and grown on uncoated BK-7 glass-coverslips (with refractive index $n_1 = 1.5224$). To label the granules, cells were incubated for 2–12 minutes with 2–5 µM acridine orange (Sigma, St. Louis, Mo. USA) added to the cell culture medium at 37 °C. Before the recordings, we washed the dish with extracellular buffer containing no dye. Dye was not present in the extracellular space after the transfer of the cells to the microscope. We did not observe any significant leakage of dye during the experimental period. Membrane fusion results in the release of the acridine orange along with the contents of the granule (Oheim et al. 1998b; Steyer et al. 1997). The dilution leads to the de-quenching of acridine orange fluorescence (Moulik et al. 1976; Palmgren 1991; Zelenin 1993) so that the signal increases temporarily, before the dye dissipates into the extracellular space. This event is observed as a brief bright cloud on time-resolved fluorescence images (Oheim et al. 1998b; Steyer et al. 1997).

Viewing individual granule motion

Experimental procedure

The coverslips with adherent cells were inserted into a custom-built holder and placed on the fixed stage of an upright microscope modified for EW excitation (Oheim et al. 1998a). Before switching to EW illumination, cells were briefly viewed by bright-field and epifluorescence illumination to verify cell adhesion and staining. Fluorescence excitation was shuttered except for periods of image acquisition. All experiments were performed at room temperature (20–23 °C). During the experiments, the cells were perfused with external buffer [145 mM CsCl, 10 mM HEPES (pH 7.2), 2.8 mM $MgCl_2$, 2 mM $CaCl_2$, 10 mM glucose]. Slightly hypo-osmotic (315 mosm) solutions were found to improve the cells' ability to stick to the substrate. We used a Cs-based solution to reduce ionic conductances.

A high-potassium extracellular solution was locally applied from a stimulation pipette to depolarise the membrane, evoke Ca^{2+} influx through voltage-activated Ca^{2+} channels and trigger exocytosis. Stimulation buffer contained varying amounts of KCl, (145 − [KCl]) mM CsCl, 10 mM HEPES (pH 7.2), 2.8 mM $MgCl_2$ and 2 mM $CaCl_2$. We did not measure the intracellular

$[Ca^{2+}]_i$, but from the measured rate constant of granule fusion and Eq. 6 on page 106 in Heinemann et al.'s work (1993), we estimate that 8 s stimulation with 60 mM K^+ resulted in a $[Ca^{2+}]_i$, of $\sim$1.3–1.7 μM. In some experiments, intracellular solution containing varying amounts of calibrated $[Ca^{2+}]_i$ (Oheim et al. 1998b) was loaded in the whole-cell configuration of the patch-clamp technique.

EW microscopy with adjustable angle-of-incidence

We used the 488-nm line of an Ar^+ ion laser in the prism configuration of EW microscopy (see Oheim et al. 1998a, 1998b for a detailed description). This technique allowed the extent of the illuminated layer of cytosol to be modified for optimal image contrast by varying the beam angle (Oheim et al. 1999b). Under software control, we chose a penetration depth so that granules were resolved as individual pinpoints. Usually, this corresponded to an angle θ of 66–68°, with a penetration depth (1/e decay) of $\sim$103–113 nm [calculated according to Eq. 2 in Oheim et al. (1999b)] with $\lambda = 488$ nm, $n_1 = 1.5224$, $n_2 = \sim 1.36$. We used a 60×0.9 NA LumPlan water-immersion objective (Olympus, Hamburg, Germany) located opposite the prism and a $2\times$ tube lens. Images were acquired from subregions of a 512×512 pixel chip with a 16-bit air-cooled charge-couple device (PentaMax, Princeton Instruments, Trenton, NJ, USA) operated in the frame-transfer mode. To elevate the faint signal integrated during short exposures over the dark noise of the camera, we used a GenIV image intensifier that was directly fibre coupled to the CCD chip. The effective pixel size, taking into account the "honeycomb" structure of the microchannel plate, was 22.4 μm, corresponding to 186 nm in the object plane. The field of view was maximally 95×95 μm.

Measuring the penetration depth

We measured the functional dependence of the penetration depth of the EW on the angle of incidence (cf. Fig. 5 in Oheim et al. 1999b). Fluorescent 100-nm latex microspheres, some adsorbed on the coverslip, served as a reference for the axial position of the interface. Others were sprinkled over the surface of cells grown on the coverslip. One bead attached to the tip of a patch pipette, mounted on a calibrated piezoelectric manipulator, served as a moving probe for the near-field intensity (Oheim et al. 1999b). Stepping the focus up and down with the piezoelectric focus drive, we acquired images of the beads which became brighter when they came into focus and appeared dimmer when they were out of focus. The maximum of the axial fluorescence profile determined the position of the beads. The fluorescence intensity of the probe was plotted against the separation distance, and the data (for $z > 50$ nm) were fitted with a falling single exponential (Oheim et al. 1998b; Steyer and Almers 1999).

Three-dimensional granule tracking

We quantified the mobility of chromaffin granules in a $\sim$200-nm $(1/e^2)$ cytosolic layer below the plasma membrane by analysing single-granule trajectories in three-dimensional (3-D) space. Separate analysis of the "centre-of-fluorescence" in the single-spot intensity distribution and fluorescence intensity resulted in estimates for the lateral and axial particle position, respectively. A macro (Universal Imaging, West Chester, Pa., USA) recognised, located and tracked the individual spots from image to image. Once several 2-D trajectories were obtained, they were analysed in conjuction with the raw data images. Positional data and fluroescence readings were transferred into IGOR (Wavemetrics, Lake Oswego, Ore., USA) for further analysis.

Analysis of lateral granule position: centre-of-fluorescence coordinates

Raw fluorescence data were prepared for automated tracking of the lateral granule position similar to Gosh and Webb (1994). In each image of the stack, the local mean was removed by a convolution with a 3×3 Laplacian filter (Inoué 1986), and the result was spatially low-pass filtered at $\sim$1 μm^{-1}. Images were thresholded at an intensity exceeding the saddle joining the two particles (see Fig. 2A). The automated tracking of granule positions involved the iterative application of two steps: the first indentified a 7×7 (1.31 μm^2) pixel-sized search object and an extended search region (27×27 pixel) in the current image, and the second one matched the objects found in the subsequent image with those identified in the current image (Fig. 2D). The lateral granule position $(\hat{x}, \hat{y})$ of the fluorescent spot

$$\hat{x} = \sum_{x,y} x(\tilde{F}(x,y) - F_T)/\sum_{x,y}(\tilde{F}(x,y) - F_T),$$
$$\hat{y} = \sum_{x,y} y(\tilde{F}(x,y) - F_T)/\sum_{x,y}(\tilde{F}(x,y) - F_T)$$

$$(1)$$

was defined by analogy to centre-of-mass coordinates in classical mechanics. In Eq. (1), $\tilde{F}$ is the filtered fluorescence intensity and F_T is the threshold intensity.

Estimation of axial granule displacement by "local" coordinates

Non-linear filtering not only clears up the image from intracellular background and highlights particle positions but also changes the relative fluorescence intensities of neighbouring granules (see Fig. 2A, B). We obtained the axial granule positions directly from the
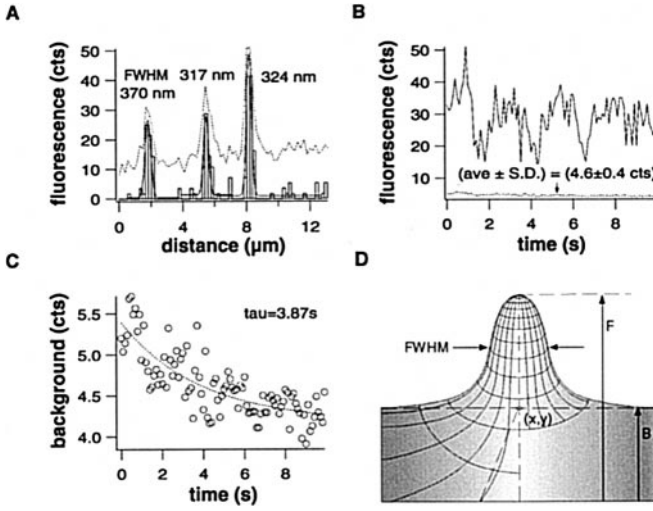
Fig. 2A–D Analysis of EW-excited fluorescence using local coordinates. **A** One-dimensional cross-section through an EW-excited chromaffin cell. Granules appear as *spikes* in the line-scan. Traces show the intensities as raw data (*dotted line*, note the signal increase in propagation direction of the evanescent field; see main text and Fig. 5), and after filtering (*open bars*). Gaussian fits to the distributions are shown as *solid lines* **B** Time-resolved fluorescence traces from a central 3×3 pixel region of a fluorescent spot (*solid line*) and its local background average (*dotted*). The background, shown on an enlarged scale in **C**, was calculated as a radial average by fitting the fluorescence data with a two-dimensional Gaussian distribution; the fit parameters are shown in **D**

raw fluorescence data intensities, averaged over a central 3×3 pixel region of the fluorescent spot. In each image, the peak position $(\hat{x}, \hat{y})$, intensity F, half-maximal width of the intensity distribution, and the local background B of many granules were obtained simultaneously (2-D). The *change* in axial position was calculated as

$$Z_n = z_{n-1} - z_n = -d \ln(F_{n-1} - B_{n-1})/(F_n - B_n) \qquad (2)$$

where F_n and B_n are the signal and background, respectively, in frame n. We estimated positional accuracy as described in the Appendix. The 3-D trajectory of the granule over the observation time was used to derive further information on the type of motion (Crank 1975). Averaging the displacement over the granule's entire trajectory in a time interval Δt yielded the mean squared displacement (MSD) (Qian et al. 1991) that was plotted against the time interval Δt, and fitted with the analytically derived diffusion equations for different types of motion; see Appendix and Crank (1975). We estimated trajectories of single granules from time-lapse sequences of 100 up to 2000 images. To reduce the total light-dose, long-range granule motion was explored from time-resolved whole-cell images recorded at 10 Hz. To study high-frequency motion for $\Delta t \to 0$, small regions of interest – usually containing two or three granules – were imaged at a frame rate of 200 Hz. The higher time-resolution data enabled us to investigate the dither of docked granules at their binding site as a function of time and in response to variations of the physiological parameters.

Results

Our aim was to study, in 3-D space, the mobility of near-membrane large-dense core granules prior to and during stimulation of exocytosis in live chromaffin cells and to investigate interactions of the granule with actin filaments. We used EW illumination to excite granular fluorescence in a thin optical section of the cytosol of cells adhering to glass coverslips. Before studying single-granule events, we evaluated the effect of varying the thickness of the illuminated layer on the image quality to define optimal observation conditions.

Optical sectioning versus scattering: effects of frustrated total-internal reflection

We used fluorescently labelled latex microspheres to estimate the EW decay as a function of the distance from the interface, z. With the 0.9-NA objective used, the intensity of the EW decayed exponentially for $z > \sim 50$ nm (rhomboids in Fig. 3A, panel 2). The collected fluorescence does not increase for smaller distances because of the distance-dependent emission pattern of the dipole and the finite solid angle of collection (panel A_1). The collection efficiency $Q(z)$ is a function of the fluorophore distance from the interface and measures the fraction of radiation captured by the 0.9-NA lens (see figure legend for details). The calculated excitation intensity $I(z)$ (solid) and the expected fluorescence signal $I(z)Q(z)$ (dotted) are superimposed on the graph. The fit of a falling exponential with date is shown as a dashed line. The 1/e decay constants for different beam angles and different refractive indices are shown in Fig. 3B. For the glass/liquid interface, the measured decay lengths closely reproduced the calculated curve over a wide range of incidence angles (open circles and solid line). For a given angle of incidence the signal decreased rapidly with distance from the interface, so that the bead was indistinguishable from the background signal due to read-out noise at a distance corresponding to two decay lengths. Optical sectioning increases rapidly for beam angles between 63° and 66°, with little gained by further increasing the angle-of-incidence.

The intracellular decay substantially differs from the result obtained for the bare glass/water interface

When the same experiment was repeated with a bead pushed through the upper membrane of a chromaffin cell (open boxes in of Fig. 3B), or beads dispersed on a flat red-blood-dell ghost on the coverslip to mimic the effect of the cytosol (solid dots), the fluorescence intensities corresponded less accurately to the theory. At all distances from the interface the measured values were higher than predicted, and the signal grew faster with
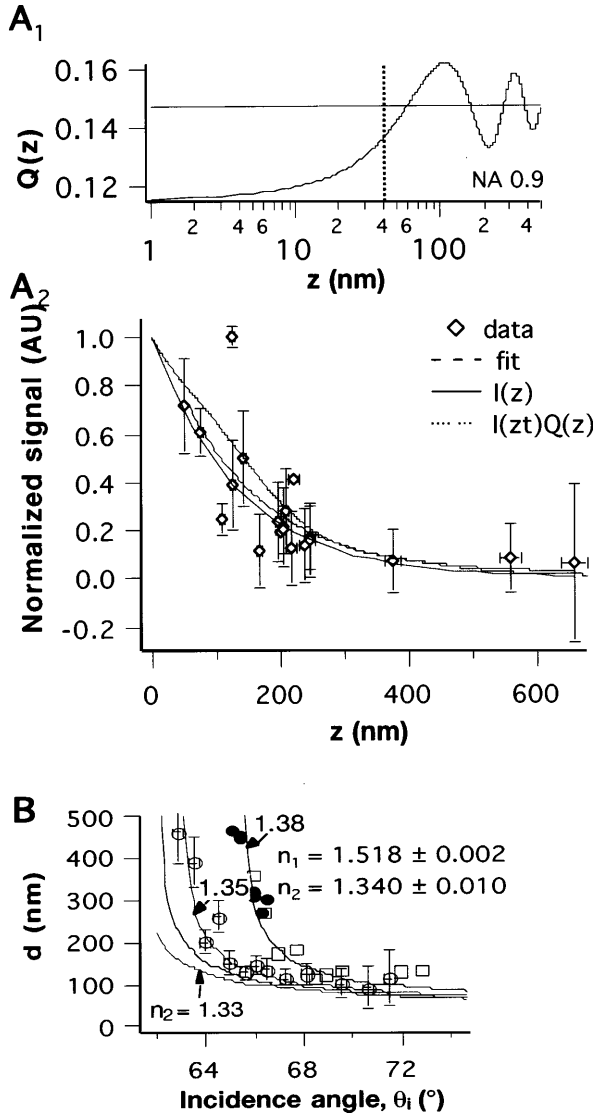
A₁

A₂

B

◄

Fig. 3A, B Calibrating the EW field-excited fluorescence. A_1 The distance-dependent collection efficiency measures the fraction of the total energy dissipated by a fixed power dipole into the solid angle captured by the 0.9-NA objective above the interface. The non-linear function incorporates both far-field and near-field effects due to interaction of the fluorophore with the interface. We assumed s-polarised light and random dipole orientation. The turning point of the curve is at 42 nm, the asymptote for $z \rightarrow \infty$ is 0.147. A_2 Decay of the EW-excited fluorescence with distance from the reflecting interface. *Rhomboids*: the measured fluorescence at distance a, $F(a;R)$, was normalised with the fluorescence of a 100-nm reference bead, $F(0;R)$. λ was 488 nm, the incidence angle $\theta = 66.5°$. Data points were best described by a falling exponential with a space constant of 129 ± 13 nm (*dashed line*). The calculated penetration depth d of the evanescent excitation intensity $I(z)$ was 110 ± 17 nm (*solid line*). The *dotted line* shows the calculated curve $I(z)Q(z) \sim F(z)$; note the deviation from the falling exponential at lower values of z. **B** Penetration depth $d(\theta; n_2)$ for different beam angles. *Solid* and *dotted lines* represent calculated values, *open circles* stand for the measured $1/e$ decay lengths of the evanescent field at the BK-7/solution interface. Owing to the uncertainty of the cytoplasm's refractive index, calculated values fall within the dotted lines. *Solid dots* represent data obtained from fluorescent beads sprinkled over a red blood cell ghost. Penetration depths are consistently higher, as is expected from the refractive index n_1 of the cell, presumably due to scattering at intracellular dielectric boundaries. *Open boxes* indicate measured decay lengths from experiments, in which a bead was pushed through the upper membrane of a chromaffin cell. The data points were best described when a homogeneous cytosolic refractive index of 1.38 was assumed, but a single exponential is insufficient to represent the data.

photons with the cytoplasm (Bryngdahl 1973). To test this hypothesis, we estimated the deformation of the evanescent wavefront due to the presence of a chromaffin cell (Fig. 4A). When the unstained cell was bathed in an extracellular solution containing fluorescein, the footprint of the cell appeared as a dark but not completely opaque shadow (Fig. 4B). Even at small penetration depths of ~200 nm, a faint comet was visible in the extracellular space on the side opposing the direction from which the beam entered the sample (Fig. 4C). In a cell stained with a cytoplasmic Ca^{2+} indicator, the intracellular background and light scattering increased with increasing d, predominantly in the propagation direction of the evanescent wave (panel C). The corresponding profiles are shown in panel D; for increasing penetration depths, the linear cross-sections resemble less and less the original profile but display a systematic increase in fluorescence along the intracellular optical path.

Optimising image contrast

In terms of the ability to image single granules, these observations imply that decreasing the penetration depth affects the signal from remote granules more strongly than the signal of granules located close to the reflecting interface. Using a low penetration depth can increase image contrast, $C = S(d) - B(d)/(S(d) + B(d))$, where S is the signal of the granule and B is the signal of

increasing penetration depths than expected from the analytical expression. The intensity decay was roughly monoexponential up to calculated penetration depths of ~150 nm. At higher values, evanescent photons appeared to be predominantly scattered, so that the EW was no longer spatially confined and photon diffusion made the field decay a complicated function of the travelled distance. Assuming a cytosolic refractive index of 1.38 (solid line) yielded a better yet not satisfactory match of the experimental findings with the calculated curve.

Re-expressing the foregoing in terms of the measured penetration depths, intracellularly, the extent of the illuminated layer was larger at all angles-of-incidence than for a homogeneous dielectric with the average refractive index of the cytoplasm. This effect was more pronounced the larger the penetration depth, until the light-confinement property was almost entirely lost at beam angles below 66°. We interpret these findings as the conversion of the evanescent wave into a propagating one due to interaction of evanescent
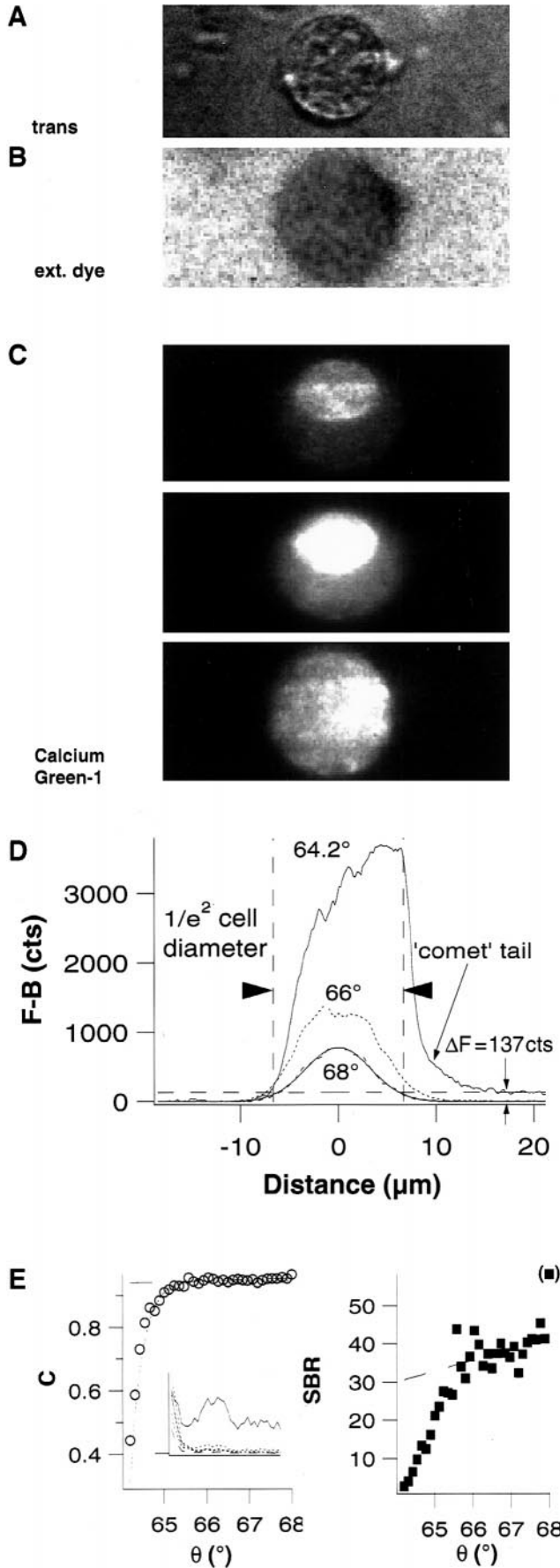
Fig. 4A–D Images of the cell/substrate contact region. **A** Bright-field transmission image of a bovine chromaffin cell of 14.4 μm diameter. **B** Using fluorescein as a water-soluble extracellular fluid marker, the cell's "footprint" on the substrate appears as a dark, almost structureless, area, into which the dye only slowly diffuses. This cell had a large footprint, almost as big as the clear cell diameter (12.2 μm). **C** The cell was then loaded with 40 μM Calcium-Green-1 in the whole-cell configuration of the patch-clamp technique, and the pipette was withdrawn after reaching a concentration equilibrium to avoid interference with the imaging. At a penetration depth of 84 nm ($\theta = 68°$, *upper panel*), the evanescent wave excites faint cytoplasmic fluorescence. The nucleus is prominent as a bright circular region. At a calculated d of 99 nm ($\theta = 66°$, *middle panel*), these features are more pronounced. When the cell is imaged at $d = 123$ nm ($\theta = 64.2°$), fluorescence increases markedly as if the fluorescence volume was less defined and photons were scattered to propagate into deeper regions of the cytoplasm. **D** The cell behaves like a lens and concentrates photons into a comet-like tail, which extends beyond the geometric limits of the cell, defined by the $1/e^2$ decay of intensity (*dashed line*). Note the offset in fluorescence, ΔF, on the right-hand side of the cell which is due to evanescent photons being converted to propagating photons. This effect is more pronounced for higher values of d (not shown). Light confinement is less well defined at higher penetration depths. **E** (*left*) Signal contribution of remote vesicles, B, relative to the signal measured at the interface, S, plotted as a contrast function of the angle of incidence; contrast is defined as $C = S(\theta) - B(\theta)/(S(\theta) + B(\theta))$. For very shallow angles of incidence, C approaches a value of 0.94. The *inset* shows the traces of S (*solid line*), various distant vesicles (*dotted*), and the unspecific background (*dashed*) as a function of θ. **E** (*right*) An alternative quantification of the image quality is the signal-to-background ratio, defined as SBR $= (1 + C)/(1 - C)$. Extrapolating the curve for shallow incidence angles to an angle of 70° one obtains a SBR of >32

more remote granules (Fig. 4E). For calculated penetration depths smaller than 100 nm, the signal-to-background ratio (SBR) saturates because the conversion of "evanescent" photons to "propagating" photons (Carniglia et al. 1972) is less of a concern. Thus, there is a limit to minimising the penetration depth because, as the penetration depth becomes considerably smaller than the depth-of-field, the background and signal decrease almost concomitantly, and the signal drops without further gain in the SBR, so that the detector's noise floor becomes limiting (Fig. 4E).

In summary, when imaging individual granules, calculated penetration depths smaller than ~130 nm – corresponding to incidence angles larger than ~66° on our setup – guaranteed a powerful optical sectioning and low photobleaching in deeper cytosolic regions at reasonable signal levels. EW-excited fluorescence intensities followed the exponential decay only in a very narrow window of penetration depths, 80 nm $< d < 130$ nm, and only there provide reliable estimates for fluorophore profiles and axial granule positions.

Precision of single-particle tracking

After determining the optimal conditions for detecting individual granules, we explored the limits for resolving granule mobility in the near-membrane region. Lateral

tracking precision is bounded by the ability to determine a peak in the intensity distribution of a diffraction-limited point image, by the detection noise, mechanical vibrations of the microscope and stage, and the distance travelled by the granule during the time of exposure. To estimate our accuracy for determining lateral particle position, a suspension of 100-nm beads was dispersed on the coverslip. The gain of the image intensifier was adjusted to provide a SNR similar to that in images of chromaffin-cell granules. Peak intensities were in the order of 2700 cts, so that the shot noise (47 cts) permits a best estimate at $\sim$2%, i.e. 3 nm, axial-positional uncertainty. Images were taken at 200 Hz. The lateral positions of an isolated stationary bead at the interface fell within a region of 56×70 nm about the mean position with no indication of drift or systematic vibrations (evidenced by autocorrelation, not shown). Standard deviations about the average bead position $(x, y) = (0, 0)$ were 16 nm in the x and 20 nm in the y direction, respectively. The axial displacement was calculated according to Eq. (2) from the fluorescence signal taken from the central 3×3 pixel region of the bead and was <5 nm. Lateral and axial displacements were used to estimate the 3-D frame-to-frame displacement, Δr, which was 30 ± 16 nm (mean $\pm$ SD). The minimal short-range diffusion coefficient was derived from the slope of the plot of the mean squared displacement (MSD) versus time interval Δt_n (in the range $0 - 0.6$ s) and was $5.73 \pm 1.33\,10^{-13}$ cm^2 s^{-1}. Thus, the minimum resolvable displacement is $\sqrt{6D_{min}^{(3)}\Delta t}$, which is in the order of $\sim$8 nm for images acquired at 5 Hz and $\sim$1 nm at 200 Hz. For $\Delta t_n \to \infty$, the MSD approached the asymptote $1.37 \pm 0.29\,10^{-11}$ cm^2 (Eq. 10; see Appendix), as if the midpoint of the bead moved within an area of 37 ± 18 nm radius, consistent with the previously observed lateral positions. This value sets the lower limit for the structures likely to be resolved in confined Brownian motion. For comparison, the free diffusion coefficient of a 100-nm bead floating in water at 20 °C is $D = kT/(6\pi\eta R)$ which is 2.09×10^{-8} cm^2 s^{-1}, and given by the Stokes-Einstein relation, where $\eta = 1.025 \times 10^{-3}$ N s m^{-2} is the viscosity of water at 20 °C, and k is the Boltzmann constant. Having a 2×10^5 times smaller diffusion coefficient, the bead obviously stuck to the coverslip. Its movement represents the lower resolution limit of our mobility measurements.

Single granule events in resting cells

EW imaging highlights individual fluorescent spots that were previously identified as individual granules (Oheim et al. 1998b; Steyer et al. 1997), with the strongest support coming from the Ca^{2+}-dependent loss of spots in response to stimulating exocytosis (refer to Oheim et al. 1998b; Steyer et al. 1997 for a detailed discussion). At an incidence angle of 66.5° (calculated $d = 110 \pm 17$ nm), the measured depth was 147 ± 33 nm, so that granules located at distances larger than $\sim$300 nm from the re-

flecting interface were virtually indistinguishable from the background.

### Vesicles in pre-exocytic states: general picture

While in a previous study our interest was to trace individual *fusion* events (Oheim et al. 1998b) and to relate the kinetics of release to dynamic changes in the near-membrane vesicle population (Oheim et al. 1999b), here we focus on the mobility of granules released at sufficiently late times that allowed a detailed analysis of the granule's preceding trajectory. The main results of our previous studies are summarised as follows:

1. Fusion was not observed in the absence of stimulation. Depolarisation of the cell evoked an increase in intracellular [Ca^{2+}]$_i$ that triggered the exocytosis of granules at the membrane surface (Oheim et al. 1999b). Maintained or repetitive membrane depolarisations gradually depleted the membrane of releasable granules.
2. Fresh granules repopulated the membrane in a dynamic equilibrium. When ongoing exocytosis reduced the population of immobile granules, the rate of supply increased. Elevation of [Ca^{2+}]$_i$ increased both the rate constants of granule fusion and supply (Oheim et al. 1999b). Newly arriving granules preferentially docked at sites where other granules already had exocytosed (Oheim et al. 1999b). Cells fully recovered from stimulation with a time constant of $\sim$5–6 min (Oheim et al. 1998b); see also Steyer et al. (1997) and Steyer and Almers (1999).

Here, we complement these observations by a detailed investigation of the mode of motion in immediate vicinity of the plasma membrane.

3. We find different components of mobility that are superimposed to constitute the granules trajectory.
4. We observed that mobilised granules often approached the membrane at an angle >45° and in a directed manner.
5. We also observed that the distribution of travelled angles and frame-to-frame displacements depended on the state of polymerisation of F-actin.
6. In contrast, docked granules showed a definite, but highly limited, mobility that was explained by Brownian motion of the anchored granule, and that was not influenced upon treatment of the cell with substances changing the degree of actin polymerisation.

Quantifying individual granule motion

Figure 5A shows an example of the time-resolved fluorescence intensity (top), the granule displacement (shown separately in axial and lateral directions, middle), and the estimated diffusion coefficient for a single

Fig. 5A–D A vesicle undergoes reversible transitions between states. Average fluorescence over 20 s, measured from the central 3×3 pixel region as running average over five frames (i.e. $F_n = \Sigma(F_{n-2} \ldots F_{n+2})/5$. The diffusion coefficient $D^{(3)}$ was determined from the $\Delta t \to 0$ approximation of the MSD plot for the intervals between the dashed lines. **A** Average fluorescence over time. Stretches of the curve that were used to define "states" are separated from phases of transition between states by *dashed lines*. The time of appearance of the cloud is indicated by an *asterisk*. Based on the in situ calibration, the distance between the two steady-state levels of fluorescence was estimated to be ∼50 nm. **B** Plot of the average 3-D diffusion coefficient over time. Same scale as in **A**. **C** The same data as in **A** and **B**, now plotted parametrically as $\log[D^{(3)}(t)]$ versus $F(t)$. Points appear to be clustered in two states. **D** Frame-to-frame displacement $r^{(3)}(\Delta t_{n=1})$ (nm) vs. the angle y of the movement with the interface (90° = perpendicular)
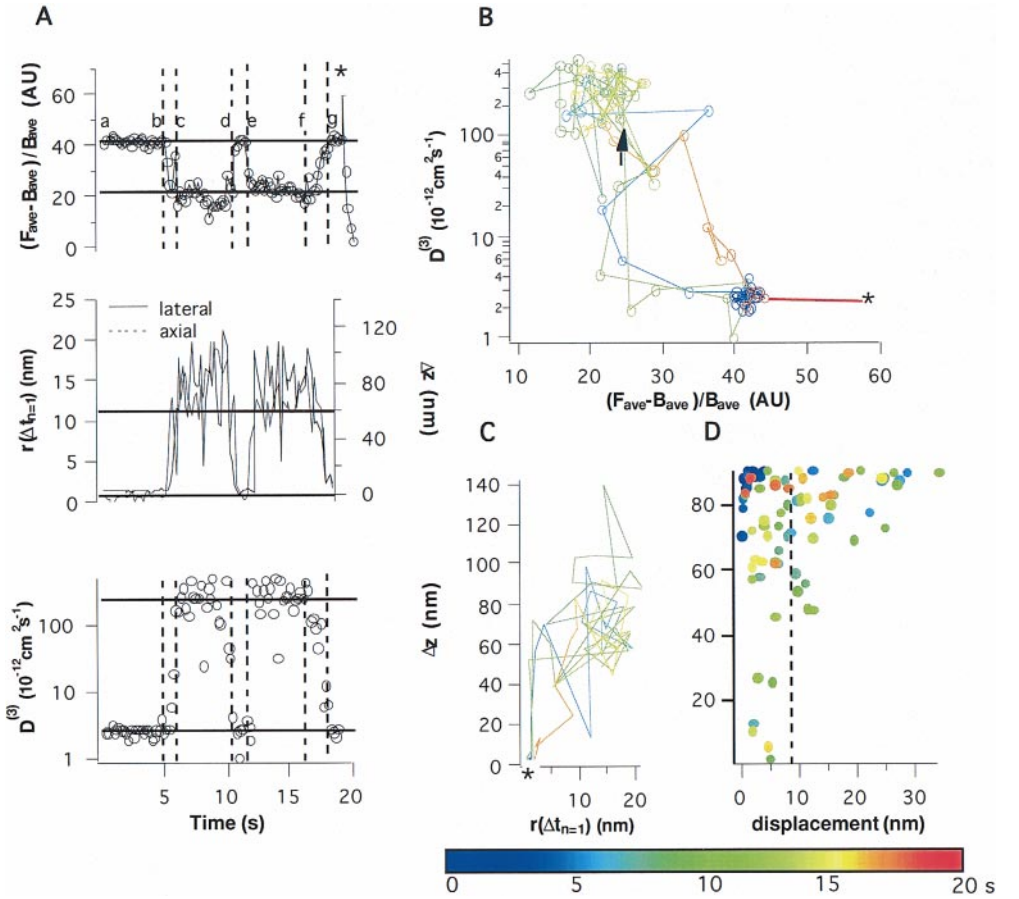
granule (bottom), plotted as a function of time (Oheim et al. 1999b). A low-noise estimate of the pair $(F, D^{(3)})(t)$ was obtained from a running average over five consecutive images. To estimate the diffusion coefficient, t_n was set to 0, and the MSD calculated over the interval $[t_n, t_n + \Delta t_n]$, where $t_n + \Delta t$ is the time of the subsequent transition of the granule to a different level of mobility, indicated by the vertical dashed lines in Fig. 5A. Fluorescence intensites and 3-D diffusion coefficients that were obtained from the analysis of stretches of the trajectory are summarised in Table 1. The granule alternated between two levels of fluorescence (Fig. 5, top) while at the same time switching from a state of high mobility to a mobility 100 times lower (bottom). A loss of mobility in the axial direction was always accompanied by a slow down in lateral mobility, and vice versa (middle). The different functional states are more evident when F and $D^{(3)}$ are plotted parametrically (Fig. 5B). The time-axis is shown in pseudocolor, with blue corresponding to $t = 0$ s and red corresponding to membrane fusion after 18.6 s.

Figure 5C is a plot of the pseudo-3-D trajectory of the same vesicle as in panels A and B. The plot uses a 2-D projection into $\left(r = (x^2 + y^2)^{1/2}, z\right)$ space. Again, the time axis is shown colour coded. Note that the trajectory is much more confined in the lateral directions than perpendicular to the membrane: the standard deviations

about the average granule position over the entire trajectory, $(\bar{r}, \bar{z}) = (8\,\text{nm}, 44\,\text{nm})$, were 4 and 7 nm, in the axial and lateral directions, respectively. Interestingly, the granule returned twice to the same location at the membrane ($z = 0$) where it had been docked at the beginning of the recording, before it fused there (marked by an asterisk). The movement showed several reversals in direction. When plotting the lateral frame-to-frame displacement $r(\Delta t_{n=1}) = (\Delta x^2 + \Delta y^2)^{1/2}$ versus the axial displacement (Fig. 5C), one recognises that the total distance travelled laterally (753 nm) is about 20% of the total distance travelled axially (3.88 µm). The average modulus of the velocity was 364 ± 120 nm/s for the distant state and 19 ± 9 nm/s for the "immobile" granule state. When plotting the frame-to-frame displacement $r^{(3)}(\Delta t_{n=1}) = (\Delta x^2 + \Delta y^2 + \Delta z^2)^{1/2}$ versus the angle $\varphi = \arctan(\Delta z/\Delta r)$ with the reflecting interface, most displacements exceeding 10 nm corresponded to angles larger than 45° (Fig. 5D). Steeper angles correlated with larger frame-to-frame displacements. Close to the plasma membrane (violet, dark blue and red-orange pseudo-color) the vesicles directional mobility seems restricted so that the angles-of-approach were predominantly perpendicular to the membrane. In contrast, only 80 nm from the membrane (green and light blue dots) the granule had the freedom to move at a broader range of angles.

Functional vesicle states

In the parameter-space representation (Fig. 5B), pairs $(F(t), D^{(3)}(t))$ cluster at two distinct sites, one at the high-mobility and low-intensity end, the other in the opposite corner. We have interpreted these "clouds" in the parameter space as the indication of *at least* two distinct populations of granules, one representing a mobile state at some distance from the membrane, the other an immobilised or "docked" state in the immediate vicinity of the plasma membrane (Oheim et al. 1999b). Granules beneath the membrane located closer to the reflecting interface are more effectively excited by the EW field, and therefore display brighter fluorescence intensities. When using the intracellular calibration of the decay evanescent-field intensity (Fig. 2C), the average granule positions are ∼60 nm apart.

To verify our previous interpretation, and to derive an overall picture of the granule populations at rest and after stimulation, as well as to provide a statistically solid basis, we repeated the previous analysis for $N = 1000$ granules in $n = 141$ cells. Owing to different exposure times and concentrations of acridine orange, different gains were used for image acquisition, so that the relationship between fluorescence intensity and axial distance was not identical from cell to cell. Therefore, only granule mobilities and positional *changes* are reported (Tables 1 and 2). As an example, the results from $N = 50$ granule trajectories in one cell are listed in Table 2 (see Fig. 6). The analysis confirms discrete distributions of both F (Fig. 6B$_1$) and $D^{(3)}$ (Fig. 6 B$_2$).
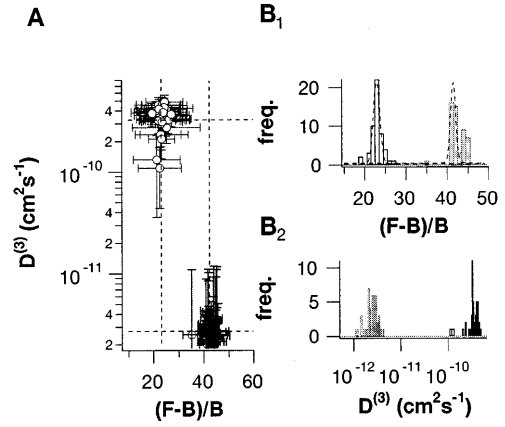

Fig. 6 A Distribution of vesicle mobilities and fluorescence intensities of $N = 50$ vesicles from the same cell as in Fig. 5. Parametric plot of the 3-D diffusion coefficient, $D^{(3)}$, and the average fluorescence F in a bovine chromaffin cell reveal two clusters of pairs. The *error bars* give SDs. **B$_1$** Fluorescence-amplitude intensity distributions and **B$_2$** distributions of $D^{(3)}$. While the states V_1 of higher mobility and low fluorescence, and the immobilised state of high fluorescence, V_2, are well defined, a sub-division of V_2 was not statistically significant (two-tailed student's *t*-test). The low-intensity and mobility ends of the histograms are given by the detection limits of vesicles and vesicle mobility, 8 au and $5.73 \pm 1.33 \times 10^{-13}$ cm^2 s^{-1}, respectively

Correlation analysis of granule motion

Examples of granule trajectories representative for their respective "class" are shown in Fig 7. In the left column (1) shows maps of the granule trajectory, projected into the (x, y) plane. Time is colour coded, $(x, y) = (0, 0)$ corresponds to the time-averaged granule position, except

▶

Fig. 7A–D Three types of vesicles were distinguished on the basis of mobility. This figure summarises their lateral (*first column*) and tree-dimensional mobility (*middle*) as determined from a time-lapse series recorded at 10 Hz as well as the temporal autocorrelation of different parameters of mobility (*right column*). Vesicles can be grouped into two equally sized populations, one largely immobile (**A**), presumably at the plasma membrane, the other one by two orders of magnitude more mobile (**B**) and located ∼60 nm deeper within the cell. A third small population (**C**), constituting ∼3% of the total, does not fit into this pattern but displays movement in a plane close to the membrane over longer distances. Note the different scale in **C**. The panels in the third column (**A3–C3**) show the calculated power spectral density of $f(t)$, PSD $(\tau) = \left| \int_0^T f(t) f^*(t + \tau) \mathrm{d}t / \int_0^T f(t) f^*(t) \mathrm{d}t \right|$, where T is the duration of the experiment, and τ indicates the time between two observations. $f(t)$ represents the speed, lateral or axial granule movement or the angle with the membrane, as a function of experiment time t. The free diffusion coefficients, calculated from the plot of the MSD versus the time interval, were $3.21 \pm 2.88 \times 10^{-12}$ cm^2 s^{-1} for the vesicle shown in panels **A$_1$** and **A$_2$**, $3.61 \pm 0.86 \times 10^{-10}$ cm^2 s^{-1} for the mobile one in panels **B**, and $1.53 \pm 0.19 \times 10^{-10}$ cm^2 s^{-1} for the vesicle displaying large-scale movement in a ∼12-nm plane parallel to the membrane before it withdraws back into the cytoplasm towards the end of the trajectory. **D** A vesicle approaches the membrane an loses its mobility. **D$_1$** Lateral positions before (*cross hair*), and after loss of mobility (*open circles*). In terms of the SDs, the lateral mobility of the vesicle decreases by a factor of 10. **D$_2$** Calculated axial positions versus lateral displacement. The calculated SD$_z$ decreases from 14 nm to <2 nm (not resolvable). **D$_3$** Of the tracking parameters, only the axial displacement shows appreciable temporal correlation

Table 1 Particle tracking parameters[a]

Range	Diffusion coefficient $D^{(3)}$ (10^{-12} cm^2 s^{-1})	Average fluorescence $F_0 - B_0$ (cts)
a to b	2.6 ± 0.4	41.7 ± 1.0
c to d	259.8 ± 147.7	20.6 ± 4.9
d to e	2.7 ± 1.0	40.8 ± 1.6
e to f	293.4 ± 115.2	23.8 ± 2.9
g through fusion of the vesicle (star)	{2.54 ± 0.4}	42.5 ± 0.9

[a] Derived from different stretches of the curves in Fig. 5. The vesicle changes reversibly between two states of different fluorescence intensity and mobility. Ranges and abbreviations as on the graphs of Fig. 5 (cts = counts)

Table 2 Two populations defined on the basis of 50 vesicles in a single bovine chromaffin cell (Fig. 6)

$N = 50$, 1 cell, 10 Hz	V_1	V_2
$D^{(3)}$ (cm^2 s^{-1})	3.22 ± 0.13 × 10^{-10}	2.15 ± 0.60 × 10^{-12}
F (cts)	22.9 ± 1.1	41.5 ± 0.87

from panels C_1 and C_2 where it represents the starting point of the trajectory. The middle column (2) shows the 3-D movement, projected into an axial-radial 2-D space.

Three types of granule mobility

The docked granule

Figure 7A shows the dither of a presumably docked granule. Traces in panels A_1 and A_2 show apparent random motion, superimposed with a slow drift (see rainbow colour). The trajectories are constrained in a cigar-shaped volume of 200 nm $(x, y) \times 20$ nm (z). In an optical section of ~300 nm, ~50% of the entire *visible* granule population of a resting cell belonged to this class, with an average $D^{(3)} = 2.0 \pm 0.6 \ 10^{-12} \ cm^2 \ s^{-1}$. The average MSD for the immobile granule population was $2.4 \times 10^{-4} \ \mu m^2$, so that the uncertainty in determining granule position had an RMS value of ~15 nm. This

value is close to the corresponding uncertainty (MSD = $6.8 \times 10^{-5} \ \mu m^2$, <9 nm RMS) obtained from the experiments in which 100-nm fluorescent beads were used for calibration purposes (see above), indicating that the tracking precision was limited by the apparatus' vibrations rather than the available signal. The magnitude of granule movement (speed, lateral frame-to-frame displacement) and direction (angle with the membrane) showed no correlation for times larger than 600 ms. In contrast, the z-component was continuous, indicative of a slow drag (1 nm/s) in the direction of the membrane, and the corresponding autocorrelation decayed much slower (shown in red).

The mobile vesicle

Unlike the first group of stationary granules, ~47% of the entire granule population was ~100 times more mobile with an average $D^{(3)} = 3.2 \pm 0.08 \ 10^{-10} \ cm^2 \ s^{-1}$.
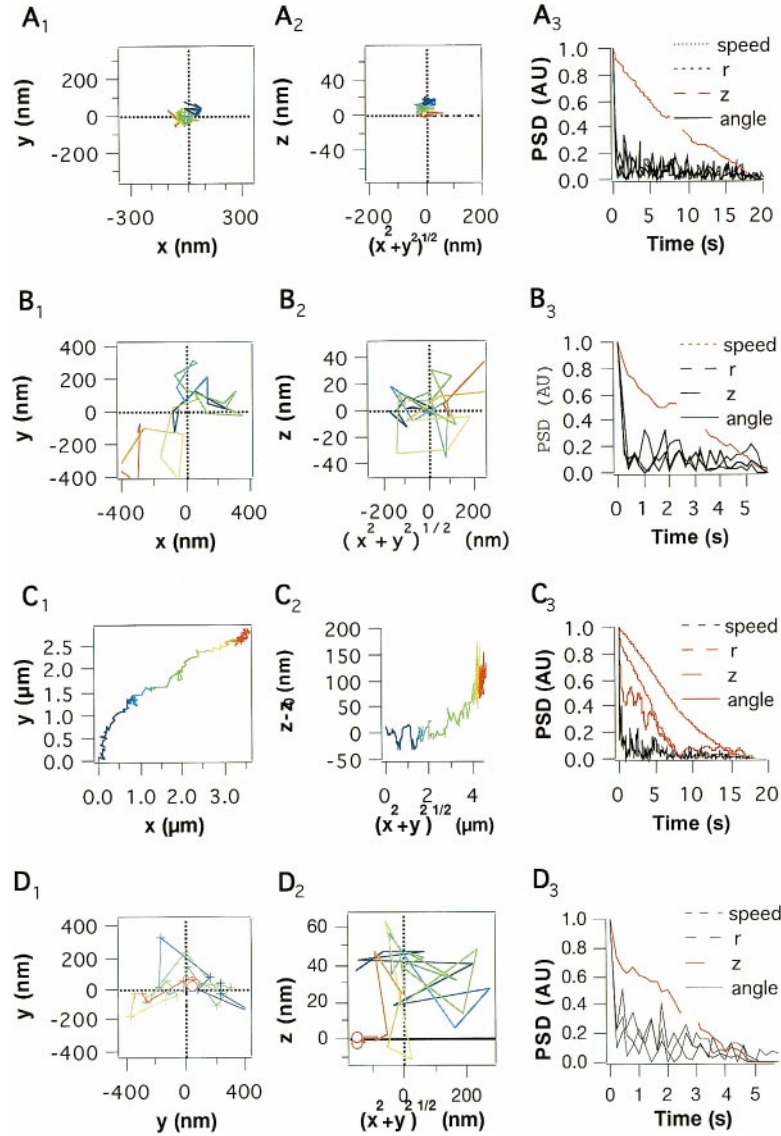
The granule's fluorescence fluctuated with an amplitude of 20–25% about a mean value that was about half the intensity of the bright, immobile granule population. An example of this population is shown in Fig. 7B, panels 1 and 2. Although mobile, the average mobility of these granules was 1/10000 of the estimate for free aqueous diffusion. Mobile granules were on average located ~60 nm deeper within the cytosol than those of the immobile population, and the midpoints slowly moved in a ~40-nm slice. Again, the correlation curves of lateral and axial mobility components and the angle with the membrane decayed within less than 600 ms, but the correlation amplitude of the granule's speed decays more slowly indicating a continuous movement.

Within the two major populations, on average, granules located at the membrane were 4.5 times less mobile in lateral and 3.7 times less mobile in axial directions than those located only a third of a granule-radius deeper within the cell, when expressed in terms of the standard deviations about the mean particle position. While exocytosis only proceeded from the bright, immobile state close to the membrane, granules frequently changed states, even in the absence of stimulation. Obviously, granule mobility reversibly changed on a length scale of hundreds of nanometres from the plasma membrane. Table 3 summarises the tracking parameters, granule density, and other findings, as well as the ratio of moving granules to immobile granules.

The rare exception

A third group of $N = 27$ granules, ~3% of the studied granule population, was observed in $n = 5$ cells (out of 141, <4%). These granules had a higher mobility and moved over micrometer distances in a ~20-nm plane close to the plasma membrane (Fig. 7C), before reascending back into the cytoplasm (panel C_2), or docking to the plasma membrane. Unlike in the earlier cases, the correlation functions of lateral and axial granule mobility and the direction travelled displayed non-vanishing amplitudes over several seconds; only the speed was correlated over less than 600 ms. Taken together, these observations indicate an active and directed but presumably discrete transport mechanism.

Angle-of-approach and number of trials before docking

Granules that entered the observed volume became brighter and lost their lateral mobility while they simultaneously reached a stable maximum intensity. Figure 7D shows an example. Tracking parameters were derived from stretches of the trajectory before and after immobilisation, indicated by crosses and circles on the graph. The short-term 3-D diffusion coefficient $D^{(3)}$, determined from the MSD plot for times $\Delta t_n < 2$ s, of this granule was $2.75 \pm 0.27 \times 10^{-10}\,\mathrm{cm^2\,s^{-1}}$ in the mobile state and $2.4 \pm 0.7 \times 10^{-12}\,\mathrm{cm^2\,s^{-1}}$ after docking. It was thus – before docking – similar to the diffusion coefficient of the mobile granule population, and decreased by two orders of magnitude, then again falling in the range of the diffusion coefficients derived previously for the stationary granules. Like most granules viewed at this penetration depth, the granule approached its binding site at an angle bigger than 45°. For ~78% of the granules ($N = 776$), the approach to the membrane was unidirectionally as if the granule's movement was

Table 3 Overview of single-granule tracking parameters in the absence of stimulation

$N = 1000$, 141 cells, 10 Hz (mean $\pm$ SD)	V_1 "mobile"	V_2 "immobile"	"Long-range movement"
Relative size	1	0.97	0.03
Membrane occupancy (%)[f]	~8%	~7%	N.D.[g]
Area density (μm^{-2})	0.7 ± 0.2	0.6 ± 0.2	N.D.
Cage radius[a] (nm)	403 ± 145	23 ± 9	~2500
Total pathlength (μm/20 s)	3.63 ± 1.00	0.98 ± 0.88	>10
Mean velocity (nm s^{-1})		44 ± 10[b]	440 ± 230
	181 ± 17	189 ± 13[c]	top up to 1100
Net velocity (nm s^{-1})		8 ± 1	260
$D^{(3)}$ (cm^2 s^{-1})	$3.22 \pm 0.13 \times 10^{-10}$	$2.15 \pm 0.60 \times 10^{-12}$	$1.53 \pm 0.19 \times 10^{-10}$
			$(5.46 \pm 6.82 \times 10^{-11})$[d]
			$(0.31\ \mathrm{nm/s})$[e]
Axial jitter (nm)	22.9 ± 1.1	~3	~12

[a] Minimal circle that contains the entire trajectory of the centre of fluorescence (assuming confined diffusion, from $t \to \infty$ approximation, Eq. A8)
[b] Slow component (assuming free diffusion, Eq. (A6), long-range diffusion coefficient form $t \to \infty$ approximation)
[c] Fast component (short-range diffusion coefficient from $t \to 0$ approximation)
[d] Assuming directed diffusion with net drift
[e] Drift velocity (Eq. A7)
[f] Estimated as follows: from morphological data, the vesicle diameter was estimated as ~300 nm. Each granule thus occupied an area equivalent to 0.0707 μm². Dence packing of vesicles would result in a maximal area density of 8–9 μm^{-2}. Multiplication with the measured average area densities of the vesicle populations gives the fractional occupancy
[g] N.D. not defined

directed, 12% ($N = 122$ granules) displayed one reversal in direction, and ~5% (48 and 54 granules, respectively) needed two or more attempts to finally bind at the plasma membrane. Very rarely (<2%), granules were seen to lift off from their docking site and move to another (not shown).

The effect of stimulation on granule mobility

General picture

With acidotropic labelling of granules, fusion is detected as the release of acridine orange into the extracellular space (Oheim et al. 1998b; Steyer et al. 1997). No spontaneous fusion events were seen in resting cells. Upon membrane depolarisation to values >0 mV, application of high K^+ or elevation of $[Ca^{2+}]_i$, cells started to secrete within milliseconds. There was no significant overall acceleration or slowdown of granule movement associated with the stimulation of exocytosis. We did not observe a net movement of near-membrane granules in the direction of the plasma membrane. These two events would manifest as a translation in the histogram of diffusion coefficients and/or fluorescence intensities. Instead, as a consequence of exocytosis and recruitment of new granules, the *number* of granules in different states of mobility changed, but the shape of the distributions and the peak position remained the same. This indicates that stimulation of exocytosis does not change the previously defined states but rather the rate constants of the transitions among these states. The analysis of $N = 1000$ granules in $n = 141$ cells confirmed our previous observation that granules undergo a well-defined sequence of steps on the way to exocytosis, and released their contents only from the immobile bright state (Oheim et al. 1999b). Assuming a linear sequential scheme, values for the rate constants relating these states were estimated at different times after the initiation of stimulation with high-K^+ and are summarised in Table 4.

Granules are targeted to their docking and fusion sites

Once in the field-of-view, mobilised granules behave like the others

Both upon stimulation and in the absence of stimulation, granules arrived at the membrane on random paths. The correlation amplitudes of the measured parameters (see above) decayed within 600 ms. Only before reaching a stable fluorescence intensity and losing mobility, we observed a net movement of "drag" in the direction of the membrane. Rarely (<2%), granules displayed significant lateral movement after docking. We observed no significant deviation from linearity in

Table 4 Rates and rate constants

	$k_1 [I] (s^{-1})$	k_1	$k_{-1} [V_1] (s^{-1})$	k_{-1}	$k_2 [V_1] (s^{-1})$	k_2	$k_{-2} [V_2] (s^{-1})$	k_{-2}	$k_3 [V_2] (s^{-1})$	k_3
Rest[a]	7.1	N.D.	7.1 s^{-1}	0.11 ± 0.05	1.5 s^{-1}	0.02 ± 0.004	1.5	0.026 ± 0.002	0	0
Stim1	9.5	–	7.1	0.11 ± 0.05	1.88 s^{-1}	0.05 ± 0.08	1.5	0.026 ± 0.002	12.1	0.11 ± 0.03
Stim2	6.8	–	7.1	0.11 ± 0.05	5.5 s^{-1}*	0.10 ± 0.009	1.5	0.026 ± 0.002	6.8	0.05 ± 0.008

[a] Transitions between pools of vesicles were determined for resting cells ("rest"), 2 s (stim1) and 10 s (stim2, * = 8 s) after stimulation with 60 mM extracellular K^+. Pools are defined in the main text, $[X]$ denotes the size of pool X as determined from the footprint region at that time. Note that $[V_1]$ depends on the penetration depth of the evanescent field such that k_2 $[V_1]$ and thus k_2 as well as $k_{-1} [V_1]$ and thus k_{-1} reflect this operational definition. k_1 was not determined (N.D.) since the size of pool I is unknown

the plot of MSD versus Δt for observation times <600 ms. For longer periods (>2 s) the MSD saturated as if granule motion was random but confined to a very limited volume of ~400-nm diameter, only slightly larger than the granule diameter, or as if the granule was tethered to some flexible "lead" of ~25 nm length. About 53% of the docked granules displayed a slow long-range motion, as indicated from the constant slope for $\Delta t \rightarrow 8$. The MSD converged to values of $D^{(2)}$ of the order of $2 \times 10^{-12}\,\mu m^{-2}\,s^{-1}$. These observations are consistent with the slow lateral diffusion of the binding site and a superimposed motion of the granule loosely attached to this site.

Sites of elevated activity

A large fraction $(\sim 60\%, N = 581)$ of the granules docked and fused at sites that had become available after fusion of a granule. We did not observe a clustering or systematic distribution of these sites of repetitive granule docking. In some cells the area density (sites/ μm^2) seemed elevated in the periphery of the cell. Additionally, at the bottom of 112 cells (out of 141, 80%) we observed regions of less than 1-μm diameter mostly located at the cell's periphery, where granules fused one after the other. The delay between the arrival of a granule and its collapse with the membrane for sites of high granule throughput was $1.00 \pm 0.28\,s$. The latency was the same when cells were bathed in 5 mM Ba^{2+} instead of 2 mM Ca^{2+}, or whole-cell patch-clamp membrane depolarisations from a resting potential of -70 mV to $+10$ mV were used for stimulation (not shown).

The role of F-actin in controlling granule mobility

The slow and constrained mobility of granules in the plane of the plasma membrane, and the non-Brownian diffusion of the mobile granules, led us to investigate the role of cortical filamentous actin (F-actin). We quantified the effect of changing actin polymerisation on granule mobility, and on the secretory response to step depolarisations.

Depolymerisation of the actin corex

When actin filaments were removed by incubation of the cell in a mixture of 5 μM latrunculin B and 700 nM latrunculin A (two compounds that stabilise G-actin), two effects were observed, depending on the length of the cells' exposure to the compounds. For exposures longer than 2–3 min, granules were seen to move out of the field-of-view in a cooperative manner (Fig. 8A). Since drug application did not interfere with the accumulation of acridine orange in chromaffin granules and the rate of photobleaching was unaffected in the presence of la-

trunculin, this result would be explained if the cells had lost adhesion. Indeed, on bright-field images, cells were seen to float in the bath. This was not due to osmotic effects, since application of latrunculin was required to trigger detachment irrespective of the osmolarity of the extracellular fluid (not shown).

Latrunculin selectively slows down mobile granules

When the cells' exposure to latrunculin was reduced to less than 2 min, the diffusion coefficient $D^{(3)}$ of the *mobile* granule population V_1 was reduced by ~50% (Table 5). Latrunculin treatment selectively affected the mobile fraction of the observed granules in a near-membrane slice, while the immobilised (and presumably docked) granules at the plasma membrane were virtually unaffected by latrunculin application. Figure 8B shows the trajectories of granules in a cell after treatment with latrunculin. Tracking parameters of $N = 225$ granules in 8 cells were determined as before in the untreated cells, and are summarised in Table 5 and Fig. 8C. The fact that granules underwent reversible transitions between the mobile and immobile granule pools indicates that the granule pools were still interchanging and may have been in equilibrium, although at a level of reduced mobility of the mobile granule fraction. We conclude that F-actin is not essential for granule movement but is likely to guide or support granule motility in a near-membrane region. Cortical actin may be required for cellular attachment to the substrate, and that these interactions are abolished when the actin meshwork is depolymerised.

Stabilisation of the actin cortex results in a complete abolition of granule movement

The weakly membrane-permeant compound jasplaki-nolide, a potent inducer of actin polymerisation, was added to the extracellular fluid in the 37 °C CO_2 incubator. Exposure of the cells for 30 min to 10 μM jas-plakinolide resulted in an almost complete inhibition of granule movement ($N = 50$ granules in 3 cells); see Fig. 8D and Table 5. Unlike with latrunculin treatment, virtually no interchange of granules between the pools V_2 and V_1 was observed. Upon stimulation of the cell by the application of 60-mM K^+ saline, the already immobilised and bright granules in pool V_2 could be recruited for secretion, but the secretory response decayed rapidly while V_2 was increasingly depleted. Most dim granules remained stationary even upon maintained depolarisation, indicating that the granules' supply to the plasma membrane was impaired (Fig. 8E). Our findings indicate that the actin meshwork's ability to reorganise is crucial for granule transport, but is not essential for secretion of a limited pool of presumably docked granules. Granule supply to the plasma membrane was almost completely removed upon stabilisation of the actin cortex. These
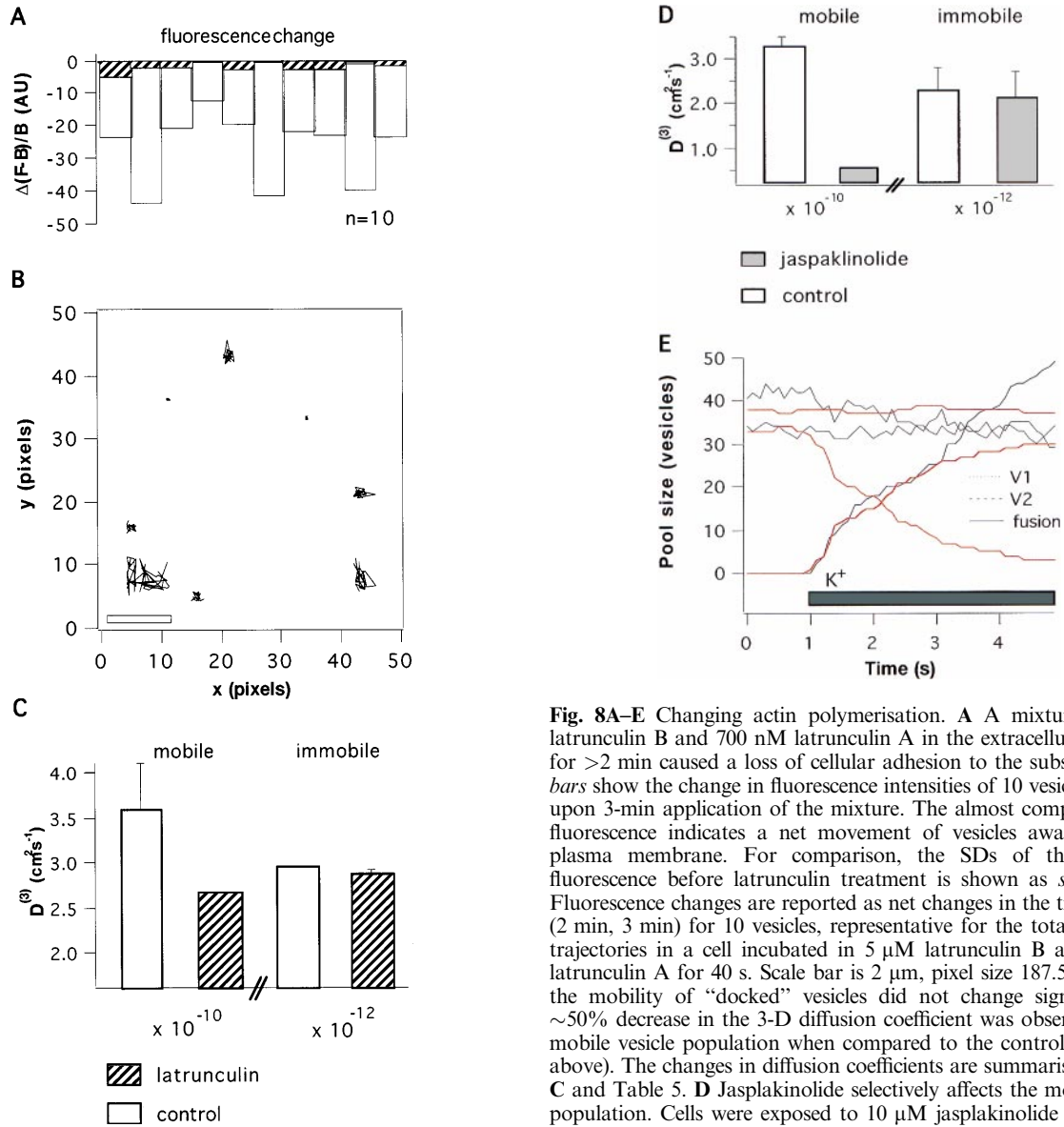
Fig. 8A–C

Fig. 8A–E Changing actin polymerisation. **A** A mixture of 5 µM latrunculin B and 700 nM latrunculin A in the extracellular solution for >2 min caused a loss of cellular adhesion to the substrate. *Open bars* show the change in fluorescence intensities of 10 vesicles in a cell upon 3-min application of the mixture. The almost complete loss of fluorescence indicates a net movement of vesicles away from the plasma membrane. For comparison, the SDs of the granules' fluorescence before latrunculin treatment is shown as *striped bars*. Fluorescence changes are reported as net changes in the time interval (2 min, 3 min) for 10 vesicles, representative for the total. **B** Vesicle trajectories in a cell incubated in 5 µM latrunculin B and 700 nM latrunculin A for 40 s. Scale bar is 2 µm, pixel size 187.5 nm. While the mobility of "docked" vesicles did not change significantly, a ~50% decrease in the 3-D diffusion coefficient was observed for the mobile vesicle population when compared to the control values (see above). The changes in diffusion coefficients are summarised in panel **C** and Table 5. **D** Jasplakinolide selectively affects the mobile vesicle population. Cells were exposed to 10 µM jasplakinolide for 30 min. After wash of the extracellular fluid, the vesicles stained with 3 µM AO for 12 min. Cells were imaged on the TIRF microscope at a calculated penetration depth of 75 nm, and the vesicle positions tracked. Exposure time was 100 ms. Time-resolved image stacks consisted of 50 images. Mobile granules were ~90% less mobile (*grey bar*) than the control population before administration of jaspakinolide (*open bar*), expressed in terms of the 3-D diffusion coefficient (*left part* of **D**), $D^{(3)}$. No obvious changes were detected for the bright, docked vesicles that were stationary (*right*). **E** Comparison of the population of the immobile bright vesicle pool V_2, the mobile population V_1 and the cumulation of fused vesicles. Under control conditions (*black*), after stimulation of the cell with 60 mM extracellular K^+, vesicles in pool V_2 were secreted, but supply of new vesicles to the plasma membrane kept the size of the population almost constant (*top, black trace*). V_1 was virtually constant in size, despite a continuous turnover of granules. After jasplakinolide treatment (*red*), secretion set on as in control conditions but levelled off after ~3 s. Pool V_1 was almost constant in size (*top red trace*), while V_2 was gradually emtied upon stimulation

observations suggest that actin does not only facilitate the delivery of secretory granules to the plasma membrane by providing filamentous rails, but that actin de-polymerisation and subsequent reorganisation is essential for granules reaching their binding site.

Discussion

We used a variant of EW imaging to study the effect of changes in the viscosity of cortical F-actin on the mobility and release of secretory granules in live chromaffin cells. We studied the interaction of evanescent photons with intracellular dielectric boundaries. Based on background-suppression considerations, images were ac-quired at a fixed penetration depth of ~200 nm intracellularly. We resolved axial granule movements of the order of 10 nm.

Table 5 Dissolution and stabilization of the actin cortex reduces the mobility of the mobile vesicle population

	0.7 μM lat. A + 5 μM lat. B	10 μM jasplakinolide, 30 min	Control[b]
$D^{(3)}$, mobile (cm^2 s^{-1})	$1.68 \pm 0.89 \times 10^{-10}$ [a]	$2.91 \pm 2.56 \times 10^{-11}$*	$3.22 \pm 0.13 \times 10^{-10}$
$D^{(3)}$, immobile (cm^2 s^{-1})	$2.01 \pm 0.91 \times 10^{-12}$ [b]	$1.97 \pm 0.73 \times 10^{-12}$*	$2.15 \pm 0.60 \times 10^{-12}$

[a] Averaged over $N = 225$ vesicles (*$N = 50$) from 8(5) cells. The values of $D^{(3)}$ were determined in the absence of stimulation
[b] Control values from $N = 50$ vesicles in one cell

Optical studies of individual granules

Conventional microscopical images resolve individual granules with varying levels of accuracy (see Angleson and Betz 1997; Betz et al. 1996; Murthy 1999; Neher 1998 for reviews): phase-based imaging provides sufficient contrast yet DIC images are hard to quantitate (Suzaki et al 1997; Terakawa et al. 1991). Hence, most authors have resorted to fluorescence techniques (Angleson et al. 1999; Burke et al. 1997; Henkel et al. 1996; Hirschberg et al. 1998; Johns et al. 1999; Ryan et al. 1997; Ryan and Smith 1995). Granules can be labelled using styryl dyes (Angleson et al. 1999; Betz and Bewick 1992), variants of GFP (Ha et al. 1996; Hirschberg et al. 1998; Kaether and Gerdes 1995; Lang et al. 1997; Levitan 1998; Wacker et al. 1997), or – less specifically – using acidophilic dyes that accumulate inside the granule lumen (Johns et al. 1999; Oheim et al. 1998b; Steyer et al. 1997).

Imaging individual granules

Out-of-focus fluorescence excitation and high granule densities near the plasma membrane have prevented resolving 3-D trajectories of individual granules in most cell types (see, however, Angleson et al. 1999). Despite their optical sectioning, confocal detection (Pawley 1995) and two-photon excitation (Denk et al. 1990) have found limited application (Burke et al. 1997; Levitan 1998; Maiti et al. 1997), as the confocal pinhole results in a very inefficient use of light which introduces a high radiation burden. Two-photon excited fluorescence is typically faint, which is disadvantageous for fast imaging of multiple sites of release at the same time.

We used a custom upright microscope for EW excitation and collected fluorescence through a water immersion objective located opposite to it. Although this configuration requires the detection of the fluorescence signal through the cell, the de-coupling of the excitation and collection pathway permits the variation of the incidence angle of the excitation light (Oheim et al. 1998a) and offers control over the penetration depth of the evanescent wave. We demonstrate that this feature becomes crucial for quantitative EW imaging.

Quantitation of EW fluorescence relies on a small penetration depth

Scattering of evanescent photons at intracellular dielectric boundaries

Setting up an evanescent field relies on refractive index differences between the dielectric media at the reflecting interface. Its field intensity decays approximately as a falling exponential (Oheim et al. 1998b). In this paper, we measure the intracellular intensity decay for different beam angles and demonstrate that, with increasing penetration, the characteristic exponential shape is gradually lost. This is particularly relevant at sites where the cytoplasm is densely packed with vesicles or granules (Parsons et al. 1995a; Plattner et al. 1997; Rohrbach 1998). The fluorescence decay is not explained by assuming a homogeneous cytoplasmic index of 1.36–1.37 (Bereiter-Hahn et al. 1979). Our findings suggest that high-contrast imaging is facilitated at *calculated* penetration depths of no more than 120 nm. In this case, we estimated an *effective* intracellular decay length of $\sim$200 nm in the cytoplasm. Smaller penetration depths would require the (combined) use of a high-refractive index substrate, like sapphire (Lang et al. 1997) or SF10, short wavelengths of the excitation light, and larger incidence angles. Similar results can be obtained by epi-excitation through the periphery of a 1.65-NA lens[1] (APO 100×, Olympus, Japan). We demonstrate that the contrast in EW-excited fluorescence images is limited by non-evanescent, i.e., propagating, field components, and that contrast saturates due to the detector's noise and low signal at small penetration depths.

Obtaining axial positional estimates

When EW field excitation is used to obtain positional information on near-membrane granules (Oheim et al. 1998b; Rohrbach 1998; Steyer et al. 1997), the accuracy of the estimate relies on the knowledge of the intracellular decay profile of the EW field. Even positional *changes* (Oheim et al. 1999b; Steyer and Almers 1999)

---

[1] After submission of this paper, Wolf Almers' laboratory presented the first application of episcopic EW excitation with a NA-1.65 objective to visualising individual synaptic vesicles in isolated bipolar nerve terminals (Zenisek et al. 1999)

can only be obtained when the exact shape is known or a monoexponential decay is assumed. This assumption is not well justified above (calculated) penetration depths >200 nm. In the absence of intracellular measurements of the EW decay, the only practical way is to associate the maximal fluorescence intensity with a location directly at the membrane, and define some distance at which granules become indistinguishable from the background, e.g., the $1/e^2$ intensity, which would correspond to roughly two times the penetration depth. In this paper, we propose a different approach in which dynamic changes in the local image background are taken into account.

Tracking individual granule movement

A number of fluorescence techniques have been developed for measurements of particle trajectories. In particular, fluorescence recovery after photo-bleaching, FRAP (Hirschberg et al. 1998; Lippincott-Schwartz et al. 1999), and fluorescence correlation spectroscopy, FCS, are widely used to measure the *average* properties of large numbers of particles (Axelrod et al. 1976; Icenogle and Elson 1983; Qian et al. 1991; Schwille et al. 1999). In these studies the behaviour of sub-populations is masked except for the distinction between mobile and (fully) immobile particles, which makes it difficult to study populations with different mobility. We used a tracking algorithm that overcomes some of these limitations and was originally introduced to analyse the mobility of membrane proteins (Gross and Webb 1986). The uncertainty in tracking ($D^{(3)} \sim 10^{-13}$ cm^2 s^{-1}) could be improved using higher detector gain, or – at the expense of photo-damage or loss of time resolution – by higher illumination intensities or longer exposure times. We wanted to make sure that our results were not confounded by photo-damage and tested for photo-destruction and photo-bleaching by three criteria. First, the MSD was continuously monitored over time as a control parameter; a systematic decrease lead to rejection. Second, after recording long image series, we elicited exocytosis by brief depolarising pulses. Third, we estimated photo-bleaching by continuously imaging a cell in the absence of stimulation. Single-granule photo-bleaching was a non-linear function of exposure time and intensity. At the light levels used, the l/e bleaching time constant was 136 s, so that we routinely recorded hundreds of images, and several trajectories consisted of 2000 exposures.

Particle recognition in EW imaging

The tracking is made difficult by the fact that a granule is an ill-defined object under conditions of EW excitation. Already, their brightness will be distributed as a function of the diameter, the penetration depth, the dye content, and their separation from the reflecting interface:

1. The diameter varies between 50 and 400 nm, with an average of about 300 nm (Loerke et al. 1999; Parsons et al. 1995a; Plattner et al. 1997).
2. Biologically identical granules may be stained differently.
3. Even for "standardised" granules, the analysis of fluorescence images would be complicated by the fact that cells do not make a flat contact with the substrate but adhere focally, while the membrane buckles up at other places.
4. EW microscopy is prone to highlight such differences. As a consequence, granules at the same distance from the plasma membrane (and presumably in the same functional state) will light up at different fluorescence intensities.

EW excitation at variable beam angles

This ambiguity can be removed using variable-angle excitation. The simultaneous estimation of multiple parameters of the fluorophore distribution (e.g., concentration, granule diameter, distance, background fluorescence) requires *at least* four independent measurements. (In practice, noise results in an even larger number of measurements.) We have shown recently that, similar to dual-wavelength ratiometric [Ca^{2+}] imaging, EW excitation at multiple beam angles can be used to eliminate unknown or variable parameters like the granule diameter and dye content (Oheim et al. 1998a). This approach, based on systematic changes of the penetration depth, allows the precise monitoring of the evolution of one or multiple parameters in isolation (Loerke et al. 1999, 2000; Rohrbach 1998). The increased spatial accuracy comes at a price, as time resolution is sacrificed for accurate localisation of the granule.

Granule mobility is restricted and not explained by free diffusion alone

3-D trajectories of individual granules were used to calculate the MSD. The type of motion of individual granules was characterised by fitting the plot of MSD versus the observation time Δt with the theoretical diffusion equations (Kusumi et al. 1993; Qian et al. 1991). Diffusion coefficients were almost four orders of magnitude smaller than the free diffusion coefficient of an equally sized sphere in aqueous solution, 1.77×10^{-8} cm^2 s^{-1} at $T = 23\,°C$. Combining a diffusion coefficient, $\sim 2 \times 10^{-12}$ cm^2 s^{-1}, and the Stokes-Einstein relation (see above), we estimate an effective viscosity of the near-membrane cytoplasm of $0.72 \pm 0.07 \times 10^{-3}$ N s m^{-2}, which is in good agreement with the estimates reported by different techniques (Bausch et al. 1998; Bicknese et al. 1993; Luby-Phleps et al. 1993) that vary around 0.85×10^{-3} N s m^{-2}, or eight times the viscosity of water. Even if granules do not move by free diffusion, $D^{(3)}$ obtained from the $\Delta t \to 0$ approximation

provides a useful order parameter for granules of different average mobility. Our estimates corroborate and extend previously reported numbers that were based on a much smaller number of granules (Johns et al. 1999; Steyer and Almers 1999). We report transport numbers (mean and net velocity, net distance travelled) that characterise the cellular transport system in Table 3. Several other characteristics of granular transport can be extracted from the MSD plot: many MSD plots saturated for $\Delta t \rightarrow \infty$. Negative curvature is interpreted as confined Brownian motion in a mesh (Faucheux and Libchaber 1994). Granule positions were constrained to a restricted are of $\sim$400-nm diameter, as if the granule was imprisoned in cage or was loosely tethered to a binding site on a $\sim$25-nm leash. It is unlikely that the "long-range" granule mobility is due to random Brownian motion alone. Indeed, the trajectories of many granules were directed to the plasma membrane, as if granules were guided to their docking sites. This interpretation is emphasised by the observation that some sites at the plasma membrane were preferred over others in a non-random manner (see also Oheim et al. 1999a). When $N = 200$ granules are placed randomly on a rectangular grid of the size of the membrane facing the coverglass, and sites can be used several fold, the probability of the observed docking pattern $\sim$10^{-5}.

Functional pools of granules

Unlike the approach of Steyer and Almers (1999) and Merrifield et al. (1999), who used episcopic EW illumination with a larger penetration depth ($\sim$640 nm), or the confocal studies of Levitan and co-workers (Burke et al. 1997; Levitan 1998), we did not study granule trajectories throughout the cell (Cole and Lippincot-Schwartz 1995; Hirschberg et al. 1998; Lippincott-Schwartz et al. 1999; Merrifield et al. 1999). We used the shallow optical section to our advantage to resolve small positional changes which are magnified as a result of the steep exponential decay of the evanescent field intensity. Two populations of chromaffin granules were identified in a 200-nm slice beneath the plasma membrane. About half of the granules were almost completely immobile, with a short-range 3-D diffusion coefficient $D^{(3)} = 2.7 \pm 1.1 \times 10^{-12}$ cm^2 s^{-1}, and presumably located at the plasma membrane. If we use the density of immobilised release-ready granules in the cell's footprint region to obtain an entire membrane-surface estimate, we predict a release-ready pool of $\sim$200 granules. A second group of granules, $\sim$100 times more mobile than the "docked" granules is observed to slowly move at some 50–60-nm distance above the membrane ($D^{(3)} = 3.23 \pm 0.92 \times 10^{-10}$ cm^2 s^{-1}). Granules change between these states in a dynamic equilibrium, even in the absence of stimulation. About 1% of the granules approached the membrane and changed direction without loss of mobility. They moved back into the cytoplasm with no measurable delay at the plasma membrane. These events were distinguished from the de-staining of a granule due to exocytosis by the lack of the intensity peak associated with the cloud of released acridine orange molecules (Oheim et al. 1998b; Steyer et al. 1997). Other granules approached the plasma membrane but were then virtually stuck there in a bound state ($N = 24$, <1%). Some of them could be recruited for secretion after a long residence time, up to minutes after their immobilisation at the membrane, but others did not move at all during the time of observation. In total, $\sim$3% behaved differently from the two major populations.

Definition of functional vesicle states

While the functional grouping of granules into mobile and immobile fractions (subsequently termed V_1 and V_2) is based on the well-distinguished diffusion coefficients, fluorescence intensities and residence times, the definition of a homogeneous mobile-granule population is less obvious. Unlike the definition of V_2, that of V_1 suffers from the fact that the granules' biophysical properties are more diverse: fluctuations about the average fluorescence intensity F as well as random and directed movements are superimposed, and are typical features of mobility. Additionally, one might argue that the location of V_1 some 50–60 nm beneath the immobile population V_2 is an artefact of the optical sectioning. Data from confocal studies suggest that both mobile and immobile granules are present at larger distances from the plasma membrane (Burke et al. 1997). On the other hand, recent studies have shown that microtubule- and actin-mediated motility systems are involved in vesicular transport (Fowler and Vale 1996; Gaidarov et al. 1999; Merrifield et al. 1999; Wacker et al. 1997) and invite speculations on whether these mechanisms could be at the basis of mobile and immobile granule states (Langford 1995; Vale et al. 1996). With our present work we provide a first link between granule mobility and F-actin polymerisation.

Dynamic changes in cortical actin

The reorganisation of the peripheral actin filaments has been proposed as a prelude to exocytosis (Aunis and Bader 1988; Aunis et al. 1979; Burgoyne and Cheek 1987; Cheek and Burgoyne 1986), to direct granules (Burgoyne and Cheek 1987; Nakata and Hirokawa 1992; Steyer and Almers 1999; Trifaró and Vitale 1993), or to regulate the size of the release-ready pool (Vitale et al. 1995). It was recently also proposed for the endocytotic limb of the granule cycle (Gaidarov et al. 1999; Merrifield et al. 1999). Evidence for interactions of cytoskeleton with granules has been indirect since only secreted granules show up in standard assays of secretion (Chow and von Rüden 1995; Gillis 1994; Gillis and Chow 1997). Thus, the decrease in the secretory response

upon interference with actin, microtubules, or cytoskeletal proteins could result from interactions at different ("earlier") stages of the exocytic pathway. In this study, we demonstrate the involvement of peripheral actin at a "late" stage of secretion control.

*Dynamic changes in the viscosity of actin
are required for sustained exocytosis*

The involvement of actin bundles – stress fibres – in mediating focal adhesion has been known for a long time (see, e.g. Fowler and Pollard 1982). The lifting off of the cells during >2 min exposure to latrunculin may be a general cell toxicity effect. In contrast, stabilising G-actin and dissolving F-actin (Balguerie et al. 1999; Vaduva et al. 1997) by <2 min incubation of the cell resulted in a decrease of the mobility of the mobile granules to ~50% of its control value in untreated cells. The effect on the docked granule population was insignificant, and the initial rate of exocytosis was even slightly enhanced (not shown).

If actin would act as a barrier to diffusion, e.g., by increasing the viscosity in a near-membrane shell, latrunculin should have increased the mobility rather than decreasing it. Our observations are compatible with an interpretation that – if the granules in V_1 were driven by motors that require F-actin – actin filaments may provide tracks for the mobile granules rather than act as a mesh hindering a stochastic granule transport (Fig. 9A). When the actin cortex was stabilised by administration of jasplakinolide, we observed a near-total loss of granule movement. Both in the presence of compounds of stabilising and dissolving actin, stimulation of exocytosis released the already bright and immobilised granules. Apparently, those granules do not require any further involvement of actin to release their contents. We did not measure how much actin is de-polymerised so we cannot exclude the possibility that the applied compounds may not have reached the entire granule population.

Based on our observations, however, it is more likely that different granule populations exist. Granules located beneath the membrane could be immediately releasable upon stimulation, without further need for actin reorganisation. The moving granules may not yet have reached an actin-independent state. Within this interpretation, stimulation would trigger a space-dependent actin reorganisation to drive granule movement, e.g., to actively push or direct the granule to its docking site at the plasma membrane (see Fig. 9B, compare Fig. 7D$_2$). Whether granules change from a long-range bulk transport mechanism (DePina and Langford 1999) to a different type of motion to move to specific sites is unclear.

Any model for actin-mediated transport must explain the characteristic shape of the MSD of many granules as a function of Δt (Fig. 9A). Our findings are compatible with a picture previously suggested by Almers and co-
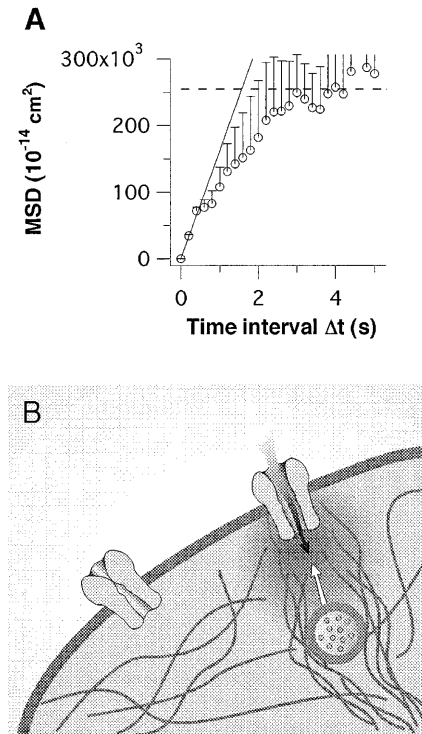

Fig. 9A, B Local time-dependent changes in the degree of actin depolymerization can result in vesicle movement. **A** Plot of the MSD versus observation time Δt for a "typical" vesicle in pool V_1 in an unstimulated chromaffin cell. The MSD curve is linear for $\Delta t \to 0$ while saturating for larger times Δt, consistent with constrained diffusion. The slope increases for shorter values of Δt. The calculated free 3-D diffusion coefficient of vesicle movement, $D^{(3)}$, was $3.21 \pm 0.86 \times 10^{-10}\ cm^2\,s^{-1}$. The radius of the "cage" restricting vesicle mobility was 505 ± 173 nm (cf. Table 3). **B** Model for vesicle movement. Actin could be both hindering and mediating vesicle movement: rapid sequential de- and re-polymerisation could be one way that actin filaments are involved in vesicle delivery to the plasma membrane and thereby modulate the secretory response

workers (Steyer and Almers 1999) in that the granule could be hindered to leave a cage-like structure of polymerised actin but nevertheless moves freely within this confined region. When the cage is moving itself, e.g., if a time- and space-dependent gradient of actin viscosity pushes the granule through the actin cortex (Fig. 9B), the result would be a slow net movement, superimposed with the fast random component of mobility within the limits of the cage. Additionally, F-actin motors would require ATP. Indeed, a complete loss of vesicular movement was observed in whole-cell experiments with no MgATP in the pipette during whole-cell patch-clamp experiments (Steyer and Almers 1999). In PC12 cells with 10 mM BDM, an inhibitor of myosin-ATP activity decreases granule mobility by ~80% of its control value (Wacker et al. 1997).

In summary, evidence is accumulating to suggest that regulated cytosolic transport occurs within an architectural framework that is likely to impose significant constraints on the diffusion of macromolecular compounds and sub-cellular organelles within the cytoplasm

(Lang et al. 1997; Luby-Phelps 1994; Steyer and Almers 1999). Fluorescent analogues of compounds that compete with actin binding or interfere with actin polymerisation will help to visualise the changes in near-membrane actin directly, while monitoring granule mobility at the same time.

Appendices

A1. Limitations to tracking precision

The tracking precision is limited by mechanical vibrations of the probe as well as by excitation intensity fluctuations, photon shot noise and detector noise. To estimate the minimal axial displacements resolved, a sequence of images was recorded of a stationary 100-nm bead located at the interface, and one located at the tip of a patch pipette at some distance from the interface (Oheim et al. 1999a). Fluorescence intensity fluctuations translate into an error:

$$\Delta Z_n = \Delta F_n/F_n d - \Delta d \ln(F_n/F_{n-1}) \tag{A1}$$

of estimating the axial granule position. F_n and F_{n-1} are defined as above, d is the length constant of the evanescent field and Δ's indicate the errors associated with their measurement.

The lateral tracking precision was determined from variations of the fitted peak position in a time series of images. Let $\langle \Delta r^2 \rangle := \langle (x_{i+1} - x_i)^2 + (y_{i+1} - y_i)^2 \rangle$; $(\langle \Delta r^2 \rangle/2)^{1/2}$ will increase for granules located at larger distances from the interface since (1) the signal S decreases rapidly with increasing distance, and (2) thresholding becomes increasingly difficult for fainter signals. As a consequence, the tracking precision varies reciprocally with the signal of the granule image as:

$$\langle \Delta r^2 \rangle/2 \approx \langle R \rangle \sigma/\bar{F} = \langle R \rangle/S^{1/2}(S + B/S)^{1/2} \tag{A2}$$

where σ and $\bar{F}$ are the standard deviation (SD) and mean of the fluorescence photon flux density over the entire spot, $\langle R \rangle$ is the first zero of the Airy pattern, S is the number of signal photons and B is the number of background photons (Gosh and Webb 1994). $((S + B)/S)^{1/2}$ is the correction factor to account for the noise contribution from the background photons B. Lower threshold values allowed no separation of neighbouring particles while higher thresholds yielded a rapid decrease in accuracy of determining particle position, because fewer pixels contributed to the calculated centre of fluorescence coordinates (Eq. 1).

A2. Random walk, mean-squared-displacement and types of motion

We analysed single-granule trajectories by calculating the MSD:

$$MSD(\Delta t) := \langle (r(t + \Delta t) - r(t))^2 \rangle_{\forall t} \tag{A3}$$

where $r = (x, y, z)$ is the position in 3-D space, and $\forall t$ indicates time-averaging over the entire duration of the experiment. In the modified equation for discrete temporal sampling of the position vector as it occurs with a CCD camera (Kusumi et al. 1993), the continuous time interval Δt is replaced by the discrete sampling interval $\Delta t_n = n\delta t$ and n and N are the number of images over which the MSD is calculated and total number of images, respectively:

$$MSD(\Delta t_n) = \frac{1}{N-n} \sum_{j=1}^{3} \sum_{k=1}^{N-n} \left\{ \left[x_j((k+n)\delta t) - x_j(k\delta t) \right]^2 \right\} \tag{A4}$$

where r is written as $(x_j)|_{j=1,\dots,3}$. Thus, the MSD for $\Delta t_1 = \delta t$ is the mean of the sum of squared displacements in 3-D space in the time interval $(0, \delta t)$, the MSD at $n = 2$ is the mean of all squared displacements in the interval $(0, 2\delta t)$ and so forth. Each point in a plot of the MSD versus Δt_n was calculated according to Eq. (A4).

Calculation of a 3-D diffusion coefficient

The lateral MSD and the fluorescence fluctuation ΔF were used to estimate the 3-D diffusion coefficient:

$$D^{(3)} \equiv d \, MSD(\Delta t_n)/(6d\Delta t_n)|_{\Delta t_n \to 0} \tag{A5}$$

from the slope of the plot of MSD versus Δt_n for $\Delta t_n \to 0$. Usually, the first 3–6 points were analysed. Additionally, the frame-to-frame displacement MSD (δt) was calculated for all times and taken as a control parameter. A continuous decrease of this number for many granules was interpreted as an indication of rundown of cell viability, and cells were excluded from the analysis.

A3. Distinguishing different types of motion

The plot of the lateral MSD versus time interval Δt_n was fitted with the theoretically derived expressions (Qian et al. 1991) to study how well different types of motion could explain the observed trajectory. As a point at time T on the plot of MSD versus Δt_n is calculated as the average over all squared displacements (Eq. A4), $r(\delta t), \dots, r(m\delta t)_{m\delta t \leq T}$, for small values of T, the MSD is averaged over more displacements than the MSDs calculated for longer observation times. In the extreme, MSD (T) is estimated from 1 value only. Therefore, the error associated with the estimation of MSD increases with Δt_n. Each point on the plot of MSD versus Δt_n was weighted with the reciprocal of their variance, and the analytically derived diffusion equations for different types of motion were fitted with the resulting curve. Free diffusion is characterised by a linear relationship between the MSD and the time interval Δt_n, with the slope:

$$D^{(2)} = d\langle l^2(\Delta t_n)\rangle/(d\Delta t) = \langle l^2(\Delta t_n)\rangle/(4\Delta t_n) \quad \forall n \quad (A6)$$

where $\forall n$ indicates averaging over all frames $n = 0, 1, \ldots, N$. Deviations from free diffusion lead to a nonlinear shape of the plot of MSD versus Δt_n. For example, directed diffusion (i.e., drift or flow with a constant velocity $V^2 = v_x^2 + v_y^2$ superimposed) results in a positive curvature as if the diffusion rate for the particle was faster the farther it had moved (Qian et al. 1991). In this case the diffusion equation becomes:

$$\langle (r(\Delta t_n) - r')^2 \rangle = \langle l^2 \rangle = 4D^{(2)}\Delta t_n + V^2\Delta t_n^2 \quad (A7)$$

The slope of a graph of MSD versus Δt_n for $\Delta t_n \to 0$ yields the 2-D diffusion coefficient (Eq. A6), but for longer times the second term will dominate the MSD, and the curve resembles a parabola. Negative curvature of the MSD versus Δt_n plot indicates that diffusion occurs not as a homogeneous process in free space but rather that its rate is lower over longer distances than over shorter distances. This behaviour results, for example, from the interactions between neighbouring granules or other mobile or immobile structures. One example of non-ideal diffusion is caged diffusion (Faucheux and Libchaber 1994; Saxton 1993; Saxton 1994). Considering the asymptotes $\Delta t_n \to 0$ (Eq. A6) and $\Delta t_n \to \infty$ yields the diffusion coefficient and the radius ρ of a circular region:

$$\lim_{n \to N} \langle l^2(\Delta t_n) \rangle = \rho^2 \quad (A8)$$

References

Almers W (1990) Exocytosis. Annu Rev Physiol 52: 607–624

Ämmälä C, Ashcroft FM, Rorsman P (1993) Calcium-independent potentiation of insulin release by cyclic AMP in single beta-cells. Nature 363: 365–368

Angleson JK, Betz WJ (1997) Monitoring secretion in real time: capacitance, amperometry and fluorescence compared. Trends Neurosci 20: 281–287

Angleson JK, Cochilla AJ, Kilic G, Nussinovitch I, Betz WJ (1999) Regulation of dense core release from neuroendocrine cells revealed by imaging single exocytic events. Nat Neurosci 2: 440–445

Aunis D, Bader MF (1988) The cytoskeleton as a barrier to exocytosis. J Exp Biol 139: 253–266

Aunis D, Hesketh JE, Devilliers G (1979) Freeze-fracture study of the chromaffin cell during exocytosis: evidence for connections between the plasma memebrane and secretory granules and for movements of plasma membrane-associated particles. Cell Tiss Res 197: 433–441

Axelrod D, Koppel DE, Schlessinger J, Elson E, Webb WW (1976) Mobility measurement by analysis of fluorescence photobleaching recovery kinetics. Biophys J 16(9): 1055–1069

Axelrod D, Hellen EH, Fulbright RM (1992) Total internal reflection fluorescence. In: Lakovicz JR (ed) Topics in fluorescence spectroscopy, vol 3. Plenum Press, New York, p 289

Balguerie A, Sivadon P, Bonneu M, Aigle M (1999) Rvs 167p, the budding yeast homolog of amphiphysin, colocalizes with patches. J Cell Sci 112: 2529–2537

Bausch AR, Ziemann F, Boulbitch AA, Jacobsen K, Sackmann E (1998) Local measurements of viscoelastic parameters of adherent cell surfaces by magnetic bead microrheometry. Biophys J 75: 2038–2049

Bereiter-Hahn J, Fox CH, Ghorell B (1979) Quantitative reflection contrast microscopy of living cells. J Cell Biol 82: 767–779

Betz WJ (1970) Depression of transmitter release at the neuromuscular junction of the frog. J Physiol (Lond) 206: 629

Betz WJ, Bewick GS (1992) Optical analysis of synaptic vesicle recycling at the frog neuromuscular junction. Science 255: 200–203

Betz WJ, Mao F, Smith CB (1996) Imaging exocytosis and endocytosis. Curr Opin Neurobiol 6: 365–71

Bicknese S, Perasamy N, Shohet SB, Verkman AS (1993) Cytoplasmic viscosity near the cell plasma membrane: measurement by evanescent-field frequency domain microfluorimetry. Biophys J 65: 1272–1282

Bittner MA, Holz RW (1992a) Kinetic analysis of secretion from permeabilized adrenal chromaffin cells reveals distinct components. J Biol Chem 267: 16219–16225

Bittner MA, Holz RW (1992b) A temperature-sensitive step in exocytosis. J Biol Chem 267: 16226–16229

Bittner MA, Holz RW (1993) Protein kinase C and clostridial neurotoxins affect discrete and related steps in the secretory pathway. Cell Mol Neurobiol 13: 649–664

Bryngdahl O (1973) Evanescent waves in optical imaging In: Wolf E (ed) Progress in optics, vol XI. North-Holland, Amsterdam, pp 169–221

Burghardt TP (1989) Polarized fluorescence emission from probes near dielectric interfaces. Chem Phys Lipids 50: 271–287

Burghardt TP, Thompson NL (1984) Effect of planar dielectric interfaces on fluorescence emission and detection: evanescent excitation with high aperture observation. Biophys J 46: 729–739

Burgoyne RD (1998) Two forms of triggered endocytosis in regulated secretory cells. J Physiol (Lond) 506: 589

Burgoyne RD, Cheek TR (1987) Reorganization of peripheral actin filaments as a prelude to exocytosis. Biosci Rep 7: 281–288

Burgoyne RD, Morgan A (1998) Calcium sensors in regulated exocytosis. Cell Calcium 24: 367–376

Burke NV, Han W, Li D, Takimoto K, Watkins SC, Levitan ES (1997) Neuronal peptide release is limited by secretory granule movement. Neuron 19: 1095–1102

Carniglia CK, Mandel L, Drexhage KH (1972) Absorption and emission of evanescent photons. J Opt Soc Am 62: 479–486

Cheek TR, Burgoyne RD (1986) Nicotine-evoked disassembly of cortical actin filaments in adrenal chromaffin cells. FEBS Lett 207: 110–114

Chow RH, von Rüden L (1995) Electrochemical detection of secretion from single cells. In: Sakmann B, Neher E (eds) Single-channel recording. Plenum, New York, pp 245–275

Cole NB, Lippincot-Schwartz J (1995) Organization of organelles and membrane traffic by microtubules. Curr Opin Cell Biol 7: 55–64

Crank J (1975) The mathematics of diffusion, 2nd edn. Clarendon Press, Oxford

Denk W, Strickler JH, Webb WW (1990) Two-photon laser scanning fluorescence microscopy. Science 248: 73–76

DePina AS, Langford GM (1999) Vesicle transport: the role of actin filaments and myosin motors. Microsc Res Techn 47: 93–106

Drexhage KH (1970) Monomolecular layers and light. Sci Am 108: 108–119

Elmquist D, Quastel DMJ (1965) A quantitative study of end-plate potentials in isolated human muscle. J Physiol (Lond) 178: 505–529

Faucheux LP, Libchaber AJ (1994) Confined Brownian motion. Phys Rev E 49: 5158–5163

Fowler VM, Pollard HB (1982) Chromaffin granule membrane-actin interactions are calcium sensitive. Nat 295: 336–339

Fowler VM, Vale R (1996) Cytoskeleton. Curr Opin Cell Biol 8: 1–3

Gaidarov I, Santini F, Warren RA, Keen JH (1999) Spatial control of coated-pit dynamics in living cells. Nat Cell Biol 1: 1–7

Gillis KD (1995) Techniques for membrane capacitance measurements. In: Sakmann B, Neher E (eds) Single channel recording. Plenum, New York, pp 155–197

Gillis KD, Chow RH (1997) Kinetics of exocytosis in adrenal chromaffin cells. Cell Dev Biol 8: 133–140

Gillis K, Misler S (1993) Enhancers of cytosolic cAMP augment depolarization-induced exocytosis from pancreatic B-cells: evidence for effects distal to Ca^{2+} entry. Pflugers Arch 424: 195–197

Glenn DE, Burgoyne RD (1996) Botulinum neurotoxin light chains inhibit both Ca^{2+}-induced and GTP analogue-induced catecholamine release from permeabilised adrenal chromaffin cells. FEBS Lett 386: 137–140

Gosh RN, Webb WW (1994) Automated detection and tracking of individual and clustered cell surface low density lipoprotein receptor molecules. Biophys J 66: 1301–1318

Gross DG, Webb WW (1986) Molecular counting of low-density lipoprotein particles as individuals and small clusters. Biophys J 49: 901–911

Ha T, Enderle T, Ogletree DF, Chemla DS, Selvin PR, Weiss S (1996) Probing the interaction between 2 single molecules–fluorescence resonance energy-transfer between a single-donor and a single acceptor. Proc Natl Acad Sci USA 93: 6264–6268

Heinemann C, von Rüden L, Chow RH, Neher E (1993) A two-step model of secretion control in neuroendocrine cells. Pflügers Arch 424: 105–112

Hellen EH, Axelrod D (1987) Fluorescence emission at dielectric and metal-film interfaces. J Opt Soc Am B 4: 337–350

Henkel AW, Simpson LL, Ridge RMAP, Betz WJ (1996) Synaptic vesicle movements monitored by fluorescence recovery after photobleaching in nerve-terminals stained with fml-43. J Neurosci 16: 3960–3967

Hirschberg K, Miller CM, Ellenberg J, Presley JF, Siggia ED, Phair RD, Lippincott-Schwartz J (1998) Kinetic analysis of secretory protein traffic and characterisation of Golgi to plasma membrane transport intermediates in living cells. J Cell Biol 143: 1485–1503

Horrigan FT, Bookman RJ (1994) Releasable pools and the kinetics of exocytosis in chromaffin cells. Neuron 13: 1119–1129

Icenogle RD, Elson EL (1983) Fluorescence correlation spectroscopy and photobleaching recovery of multiple binding reactions. Biopolymers 22: 1919–1948

Inoué S (1986) Video microscopy. Plenum Press, New York

Jahn R, Niemann H (1994) Molecular mechanisms of clostridial neurotoxins. Ann NY Acad Sci 733: 245–255

Jankowski JA, Schroeder TJ, Ciolkowski EL, Wightman RM (1993) Temporal characteristics of quantal secretion of catecholamines from adrenal medullary cells. J Biol Chem 268: 14694–14700

Johns LM, Shelden EA, Levitan ES, Holz RW, Axelrod D (1999) Motion of chromaffin granules near the plasma membrane as visualised with total internal reflection fluorescence microscopy. Biophys J 76: A70

Kaether C, Gerdes HH (1995) Visualization of protein transport along the secretory pathway using green fluorescent protein. FEBS Lett 369: 267–271

Kusumi A, Sako Y, Yamamoto M (1993) Confined lateral diffusion of membrane receptors as studied by single particle tracking (Nanovid microscopy); effects of calcium-induced differentiation in cultured epithelial cells. Biophys J 65: 2021–2040

Lang T, Wacker I, Steyer J, Kaether C, Wunderlich I, Soldati T, Gerdes H-H, Almers W (1997) Ca^{2+}-triggered peptide secretion in single cells imaged with green fluorescent protein and evanescent-wave microscopy. Neuron 18: 857–863

Langford GM (1995) Actin- and microtubule-dependent organelle motors: interrelationships between the two motility systems. Curr Opin Cell Biol 7: 82–88

Levitan ES (1998) Studying neuronal peptide release and secretory granule dynamics with green fluorescent protein. Methods (Duluth) 16: 182–187

Lippincott-Schwartz J, Cole N, Presley J (1999) Unravelling Golgi membrane traffic with green fluorescent protein chimeras. Trends Cell Biol 8: 16–20

Loerke D, Oheim M, Stühmer W (1999) Investigation of the three-dimensional distribution of near-membrane chromaffin granules using evanescent-wave microscopy. Biophys J 76: A69

Loerke D, Preitz B, Stühmer W, Oheim M (2000) Super-resolution measurements by evanescent-wave excitation of fluorescence using variable beam incidence. J Biomed Opt 5: 23–30

Luby-Phelps K (1994) Physical properties of the cytoplasm. Curr Opin Cell Biol 6: 3–9

Luby-Phleps K, Mujumdar S, Mujumdar RB, Ernst LA, Galbraith W, Waggoner AS (1993) A novel fluorescence rationmetric method confirms the low solvent viscosity of the cytoplasm. Biophys J 65: 236–242

Maiti S, Shear JB, Williams RM, Zipfel WR, Webb WW (1997) Measuring serotonin distribution in live cells with three-photon excitation. Science 275: 530–532

Merrifield CJ, Moss SE, Ballestrem C, Imhof BA, Giese G, Wunderlich I, Almers W (1999) Endocytic vesicles move at the tips of actin tails in cultured mast cells. Nat Cell Biol 1: 72–74

Moulik SP, Ghosh S, Das AR (1976) Environment-induced spectral behaviour of acridine orange dye. Indian J Chem 14: 302–305

Murthy V (1999) Optical detection of synaptic vesicle exocytosis and endocytosis. Curr Opin Neurobiol 9: 314–320

Nakata T, Hirokawa N (1992) Organization of cortical cytoskeleton of cultured chromaffin cells and involvement in secretion as revealed by quick-freeze, deep-etching, and double-label immunoelectron microscopy. J Neurosci 12: 2186–2197

Neher E (1998) Vesicle pools and Ca^{2+} microdomains: new tools for understanding their roles in neurotransmitter release. Neuron 20: 389–399

Oheim M, Loerke D, Preitz B, Stühmer W (1998a) A simple optical configuration for depth-resolved imaging using variable-angle evanescent-wave microscopy. In: Bigio EE, Schneckenburger H, Slavik J, Svanberg K, Viale T (eds) Proceedings of SPIE, vol 3568(3). pp 131–140

Oheim M, Loerke D, Stühmer W, Chow RH (1998b) The last few milliseconds in the life of a secretory granule. Docking, dynamics and fusion visualized by total internal reflection fluorescence microscopy (TIRFM). Eur Biophys J 27: 83–98

Oheim M, Naraghi M. Müller TH, Neher E (1998c) Two-dye two-wavelength measurements: results from adrenal chromaffin cells. Cell Calcium 24: 71–84

Oheim M, Loerke D, Chow RH, Stühmer W (1999a) Evanescent-wave microscopy: a new tool to gain insight into the control of transmitter release. Phil Trans R Soc Lond B 354: 307–318

Oheim M, Loerke D, Stühmer W, Chow RH (1999b) Multiple stimulation-dependent processes regulate the size of the releasable pool of vesicles. Eur Biophys J 28: 91–101

Palmgren MG (1991) Acridine orange as a probe for measuring pH gradients across membranes: mechanism and limitations. Anal Biochem 192: 316–321

Parsons TD, Coorssen JR, Horstmann H, Almers W (1995a) Docked granules, the exocytic burst, and the need for ATP hydrolysis in endocrine cells. Neuron 15: 1085–1096

Parsons TD, Coorssen JR, Horstmann H, Lee AK, Tse FW, Almers W (1995b) The last seconds in the life of a secretory vesicle. Cold Spring Harbor Symp Quant Biol 60: 389–396

Pawley JB (1995) Handbook of biological confocal microscopy, Plenum, New York

Penner R, Neher E, Dreyer F (1986) Intracellularly injected tetanus toxin inhibits exocytosis in bovine adrenal chromaffin cells. Nature 324: 76–78

Plattner H, Artalejo AR, Neher E (1997) Ultrastructural organization of bovine chromaffin cell cortex – analysis by cryofixation and morphometry of aspects pertinent to exocytosis. J Cell Biol 139: 1709–1717

Qian H, Sheetz MP, Elson EL (1991) Single particle tracking – analysis of diffusion and flow in two-dimensional systems. Biophys J 60: 910–921

Rohrbach A (1998) Fluoreszenzanregung hinter dielektrischen Grenzflächen. Univ Dissertation, Heidelberg

Rosenmund C, Stevens CF (1996) Definition of the readily releasable pool of vesicles at hippocampal synapses. Neuron 16: 1197–1207

Ryan TA, Smith SJ (1995) Vesicle pool mobilization during action potential firing at hippocampal synapses. Neuron 14: 983–989

Ryan TA, Reuter H, Smith SJ (1997) Optical detection of quantal presynaptic membrane turnover. Nature 388: 478–482

Saxton MJ (1993) Lateral diffusion in an archipelago. Biophys J 64: 1766–1780

Saxton MJ (1994) Anomalous diffusion due to obstacles: a Monte Carlo study. Biophys J 66: 394–401

Schroeder TJ, Jankowski JA, Senyshyn J, Holz RW (1994) Zones of exocytotic release on bovine adrenal medullary cells in culture. J Biol Chem 269: 17215–17220

Schwille P, Haupts U, Maiti S, Webb WW (1999) Molecular dynamics in living cells observed by fluorescence correlation spectroscopy with one- or two-photon excitation. Biophys J 77: 2251–2265

Smith C, Moser T, Xu T, Neher E (1998) Cytosolic Ca^{2+} acts by two separate pathways to modulate the supply of release-competent vesicles in chromaffin cells. Neuron 20: 1243–1253

Stevens CF, Tsujimoto T (1995) Estimates for the poor size of releasable quanta at a single central synapse and for the time required to refill the pool. Proc Natl Acad Sci USA 92: 846–849

Steyer JA, Almers W (1999) Tracking single secretory granules in live chromaffin cells by evanescent-field fluorescence microscopy. Biophys J 76: 2262–2271

Steyer JA, Horstmann H, Almers W (1997) Transport, docking and exocytosis of single secretory granules in live chromaffin cells. Nature 388: 474–478

Suzaki E, Kobayashi H, Kodama Y, Masujima T, Terakawa S (1997) Video-rate dynamics of exocytotic events associated with phagocytosis in neutrophils. Cell Mot Cytoskel 38: 215–228

Terakawa S, Fan JH, Kumakura K, Ohara-Imaizumi M (1991) Quantitative analysis of exocytosis directly visualised in living chromaffin cells. Neurosci Lett 12: 82–86

Trifaró J-M, Vitale ML (1993) Cytoskeleton dynamics during neurotransmitter release. Trends Neurosci 16: 466–472

Vaduva G, Martin NC, Hopper AK (1997) Actin-binding verroprolin is a polarity development protein required for the morphogenesis and function of the yeast actin cytoskeleton. J Cell Biol 139: 1821–1833

Vale RD, Funatsu T, Pierce DW, Romberg L, Harada Y, Yanagida T (1996) Direct observation of single kinesin molecules moving along microtubules. Nature 380: 451–453

Vitale ML, Rodriguez DelCastillo A, Tchakarov L, Trifaró J-M (1991) Cortical filamentous actin disassembly and scinderin redistribution during chromaffin cell stimulation precede exocytosis, a phenomenon not exhibited by gelsolin. J Cell Biol 113: 1057–1067

Vitale ML, Seward EP, Trifaró J-M (1995) Chromaffin cell cortical actin network dynamics control the size of the release-ready vesicle pool and the initial rate of exocytosis. Neuron 14: 353–363

Wacker I, Kaether C, Kromer A, Migala A, Almers W, Gerdes HH (1997) Microtubule-dependent transport of secretory vesicles visualized in real-time with a GFP-tagged secretory protein. J Cell Sci 110: 1453–1463

Weis S, Schneggenburger R, Neher E (1999) A model of Ca^{2+}-dependent vesicle pool dynamics and short term synaptic depression. Biophys J 77: 2418–2429

Xu T, Binz T, Niemann H, Neher E (1998) Multiple kinetic components of exocytosis distinguished by neurotoxin sensitivity. Nat Neurosci 1: 192–200

Zelenin AV (1993) Acridine orange as a probe for molecular and cell biology. In: Mason WT (ed) Fluorescent and luminescent probes for biological activity. Academic Press, London, pp 83–99

Zenisek et al. (1999) Imaging exocytosis of single synaptic vesicles by evanescent-field microscopy. Soc Neurosci Abstr 25(1): A1251